Research Square

Preprints are preliminary reports that have not undergone peer review.
They should not be considered conclusive, used to inform clinical practice,
or referenced by the media as validated information.

Waste to Nano material approach: Iron Oxide Nanoparticles synthesized from Litchi chinensis peel extract (LC-Fe2O3-NPs) for the removal of toxic dyes

Sivakumar Bandaru
Andhra University
Velaga P V S Sai Pranai
Andhra University
A. Narendra Kumar
Andhra University
Tamirat Lamaro Bate
Andhra University
Megersa Tadesse Adugna
megersata@wollegauniversity.edu.et
Wollega University
Pulipati King
Andhra University
Meena Vangalapati
Andhra University

Article

Keywords: Adsorption, Industrial dyes, Wastewater treatment, Litchi chinensis extract-Fe_2O_3-NPs, Congo Red (CR), Alizarin Red S (ARS), Response Surface Methodology (RSM)

Posted Date: April 13th, 2026

DOI: https://doi.org/10.21203/rs.3.rs-9248846/v1

License: This work is licensed under a Creative Commons Attribution 4.0 International License.
Read Full License

Additional Declarations: No competing interests reported.

Waste to Nano material approach: Iron Oxide Nanoparticles synthesized from Litchi chinensis peel extract (LC-Fe_2O_3-NPs) for the removal of toxic dyes

Sivakumar Bandaru[1], Velaga P V S Sai Pranai[2], A. Narendra Kumar[2], Tamirat Lamaro Bate[1], Megersa Tadesse Adugna[3*], Pulipati King[4], Meena Vangalapati[4]

[1]Research Scholar, Department of Chemical Engineering, AUCE (A), Andhra University, Visakhapatnam, India

[2] Department of Chemical Engineering, AUCE (A), Andhra University, Visakhapatnam, India

[3*]Department of Chemical Engineering, Faculty of Technology, Wollega University, Shambu Campus, Shambu, Ethiopia

E-mail: megersata@wollegauniversity.edu.et

[4]Professor, Department of Chemical Engg, Andhra University College of Engg, Visakhapatnam, India

ABSTRACT

The synthesis strategy concentrates on reducing the use of dangerous chemicals, using nanotechnology to clean up toxic substances in wastewater, and making sure that the produced nanoparticles have no effect in the environment. Because *Litchi chinensis* extract has good adsorptive qualities and contains phytochemicals such flavonoids, phenolics, and steroids, it was used in this study to create Iron Oxide nanoparticles. *Litchi chinensis* Iron Oxide nanoparticles (LC-Fe_2O_3-NPs) are formed as a result of these bioactive substances' natural reducing and stabilizing effects. LC-Fe_2O_3-NPs eliminated Congo Red and Alizarin Red S with efficiencies of 95.62% and 96%, respectively, at an initial dye concentration of 10 mg/L. The maximum adsorption capabilities of LC-Fe_2O_3-NPs for Congo Red and Alizarin Red S dyes were 171.23 mg/g and 186.66 mg/g, respectively. Particles with irregular shapes and sizes smaller than 100 nm. The surface appearance, elemental content, crystalline structure, and functional groups of the produced LC-Fe_2O_3-NPs were examined using SEM-EDX, TGA, XRD, FTIR techniques and XPS, BET analysis. The experiment to remove Congo Red (CR) and Alizarin Red S (ARS) dyes is based on the adsorption approach. Various parameters, including temperature, initial dye concentration, solution pH, adsorbent dosage, and agitation time, were reported and adjusted. Equilibrium data analysis revealed that the Freundlich isotherm model best explained the adsorption behavior for LC-Fe_2O_3-NPs. Additionally, thermodynamics and kinetics were examined. Response Surface Methodology (RSM) optimization studies were examined and contrasted with experimental data.

Keywords: Adsorption, Industrial dyes, Wastewater treatment, Litchi chinensis extract-Fe_2O_3-NPs, Congo Red (CR), Alizarin Red S (ARS), Response Surface Methodology (RSM).

1. INTRODUCTION

Heavy metals released into the environment have posed a significant threat to the environment and public health because of their toxicity and persistence in environment. The contamination of wastewaters and surface waters by toxic heavy metals is a worldwide environmental problem[1]. Water being the primary need for the sustenance of life on earth and access to clean and safe water is vital to secure civic health. Nanoparticles are basically used for removing pollutants including metals, nutrients, cyanides, organics, algal toxins, viruses, bacteria, parasites, and antibiotics. Mainly four types of nanomaterials are being used in wastewater treatment, e.g., metal-containing NPs, carbonaceous nanomaterials, zeolites, and dendrimers. Carbon nanotubes and nanofibers are also useful to some extent[2]. In the environment, iron plays an important role in contaminant mobility, sorption and breakdown due to its role as an electron donor (during the oxidation of Fe^{2+} to Fe^{3+}) and in its various mineral forms, as a precipitant/sorbent substrate[3,4]. It

was further estimated that around 10–15% of the dyes used in the tanning, textile, cosmetic, food, paper, plastic, and biomedical industries are lost in the effluents during the dyeing operations[5].

[1]Research Scholar, Department of Chemical Engineering, AUCE (A), Andhra University, Visakhapatnam city 530003, Andhra Pradesh State, India.[2]M Tech Student Chemical Engineering, AUCE(A), Visakhapatnam, AP, India. [3]Department of Chemical Engineering, Faculty of Technology, Wollega University, Shambu Campus, Shambu, Ethiopia. [4]Dept of Chemical Engg, Andhra University College of Engg, Visakhapatnam, India. ✉email: megersata@wollegauniversity.edu.et

The compounds which absorb electromagnetic energy in the visible range (~350–700 nm) are colored and these colored compounds are mostly known as dyes[6]. Azo dyes represent the largest production volume of dye chemistry today, and their relative importance may even increase in the future. They play a crucial role in the governance of the dye and printing market[7,8]. Many synthetic azo dyes and their metabolites are toxic, carcinogenic, mutagenic, leading to potential health hazard to humankind[9,10,11]. Textile wastewater, which is a by-product of textile industry, is a mixture of colorants (dyes and pigments) and various organic compounds used as cleaning solvents, plasticizers etc. It also contains high concentrations of heavy metals, total dissolved solids, and has higher chemical as well as biological oxygen demand. Thus, textile wastewater is chemically very complex in nature[12,13]. Azo dyes are the most widely used dyes and represent over 60% of the total dyes. . Synthetic dyes cannot be efficiently decolorized by traditional biological processes. They are complex aromatic compounds with significant structural diversity[14,15,16].

Novel-nanomaterials with superior performance are constantly applied to improve their applications in environmental pollution cleanup. Metal-organic frameworks (MOFs) with abundant functional groups and tailorable structure, have represented a new field of capturing various heavy metal ions[17]. The adsorption process provides an attractive alternative for the treatment of contaminated waters, especially if the sorbent is inexpensive and does not require an additional pretreatment step before its application. Adsorption is known to be a better technique, which has great importance due to the ease of operation and comparable low cost of application in discoloration process[18]. Alizarin Red S (ARS) is a water soluble anthraquinone dye originally derived from the root of the madder plant. It has been extensively employed since ancient times in dyeing textiles. It is a strong oxidizing agent, and hence, must be stored away from moisture and heat[19]. These dyes belong to the group of anthraquinone dyes; the most durable dyes that cannot be completely degraded by general chemical, physical, and biological processes. Their resistance to degradation is attributed to their complex structures of aromatic rings that afford high physicochemical, thermal, and optical stability[20].

The widespread practical application of metal nanoparticles (particles less than 100 nm) is attributable to a number of their unique properties. Different physical and chemical processes are currently widely used to synthesize metal nanoparticles, which allow one to obtain particles with the desired characteristics[21]. Interestingly, litchi peel has a variety of functional groups, such as carbonyl, hydroxyl, carboxyl and amino groups, and thus has potential value as novel adsorbent material. Bio sorbents derived from litchi peel and its derivatives have been used to remove dyes from wastewater. In addition, litchi peel contains a large amount of cellulose, lignin, sugars and fats, which can be used as a potential carbon source for the preparation of biochar materials[22]. CR dye ($C_{32}H_{22}N_6Na_2O_6S_2$) is an anionic acidic dye and possesses a complex chemical structure as well as composition. It is recognized as a carcinogen because it contains aromatic amines in its structure. The presence of aromatic structures makes azo dyes resistant to natural degradation. CR is reported to metabolize to benzidine and so has the potential for bioaccumulation and is difficult to remove from water. CR is commonly applied for dyeing process of yarn, which is chemically a benzidine azo dye. CR is commonly used in the textile, paper, printing, and other industries[23,24,25].

Iron Oxide is a mineral compound with several crystal structures and magnetic characteristics. There are different types of Iron Oxides, hematite (α-Fe_2O_3), maghemite (γ-Fe_2O_3), and magnetite (Fe_3O_4). These compounds have physical properties, such as crystallographic structure, magnetic, density, hardness, and color[26]. Therefore, ARS has been selected as target pollutants in many

investigations on the treatment of dye-laden wastewaters. The treatment of dye wastewater was commonly carried out by physical and chemical processes like photocatalysis, ozonation, membrane filtration, electrocoagulation, and adsorption[27,28]. Therefore, in this work, Fe_3O_4 magnetic nanocrystals are prepared and then appended to litchi peels to develop a new magnetic bio adsorbent, magnetic litchi peel (MLP), with the objective to address the issues related to the separation of bio adsorbents based on Agro-wastes in adsorption processes[29,30]. In regard to the advantages of multivariate optimization which have recently been revealed, especially experimental design rather than the conventional "one-at-a time" method has attracted interests in relation to optimization of adsorption process. It is well known that experimental design provides more information with fewer experiments, running a Response Surface Methodology (RSM) which leads to an empirical mathematical model in relation with effective variables and their interactions[31-40].

2. MATERIALS AND METHODS

Litchi chinensis peels are collected from local fruit market in Visakhapatnam, India.

2.1 Chemicals and equipment Required

Ferrous Sulphate ($FeSO_4$), NaOH, HCl, Distilled Water, Congo Red (CR) and Alizarin Red S (ARS), Conical flasks, 1-liter beaker, Measuring Jar, Pipette, Orbital Shaker, pH meter, Mechanical Stirrer, Spectrophotometer

2.2 Estimation of Dyes

Preparation of Dye Solutions

To create Stock dye solutions with a concentration of 1000 mg/L, 1 g of Congo Red and 1 g of Alizarin Red S dyes were individually dissolved in distilled water and then diluted to 1000 ml using volumetric flasks. These stock solutions were serially diluted with distilled water to create working dye solutions with concentrations ranging from 10 to 100 mg/L for experimental analysis.



Fig. 1. Congo Red Dye Solution



Fig. 2. Alizarin Red S Dye Solution

2.3 Synthesis of Litchi chinensis Iron Oxide Nanoparticles (LC-Fe_2O_3-NPs)

2.3.1 Preparation of Litchi chinensis Peel Extract

Litchi chinensis peels were obtained from a local fruit market, properly cleaned with distilled water and sun dried. After drying, the peels were ground into a fine powder. For each variety of peel, 40 g of powder were combined with 500 ml of distilled water using a magnetic stirrer and heated to 363 K for 40 minutes. After cooling the mixture was filtered via filter paper. The resultant filtrate is used to make extract of Litchi chinensis as shown in (Fig. 3).

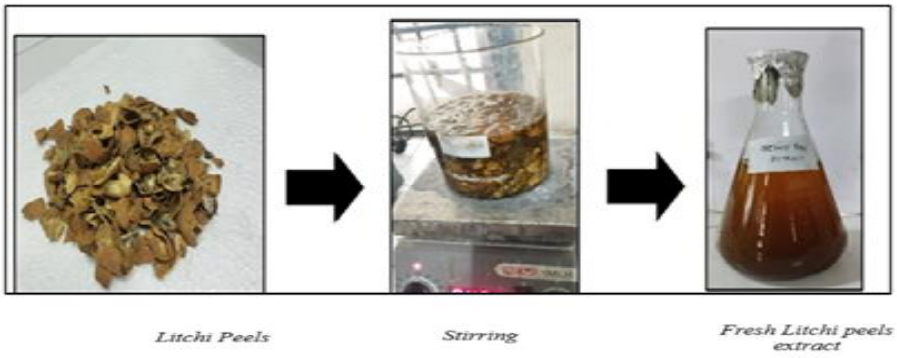


Fig. 3. Preparation of Litchi chinensis Peel Extract.

2.3.2 Synthesis of peels of Litchi chinensis Iron Oxide Nanoparticles (LC-Fe_2O_3-NPs)

To make Litchi chinensis Iron Oxide nanoparticles (LC-Fe_2O_3-NPs), the fresh Litchi chinensis peel extract and a ferrous sulfate solution were mixed in the right amounts.3.797 g of Ferrous Sulphate granules were dissolved in 1000 ml of water to create a 0.025M $FeSO_4$ solution. After that, this solution was combined in a 1:1 ratio with an equivalent volume of fresh peel extract that had already been made. A mechanical stirrer was used to agitate the mixture for half an hour at room temperature. After this time, the solution turned dark, indicating the production of Fe^{+2} ions. The solution's pH was determined and brought to 8 by adding the proper amounts of 0.1 N NaOH and 0.1 N HCl. For another 60 minutes, the mixture was mixed once more. The mixture was centrifuged for 5 min at 4000 rpm after being stirred. After that, the pellets were put on a small plate and dried for a day at 800°C in a vacuum oven. After drying, the pellets were ground into LC-Fe_2O_3-NPs using a mortar and pestle.

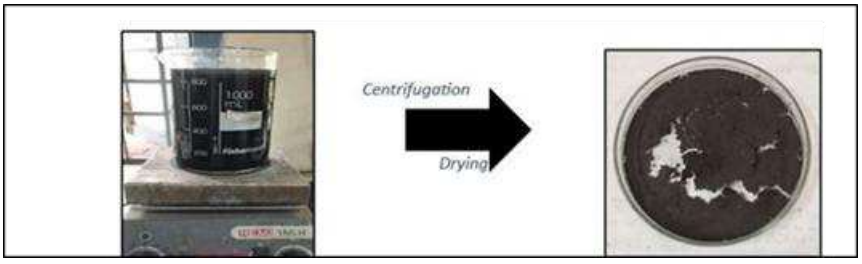


Fig. 4. Synthesis of LC-Fe_2O_3-NPs

2.4 Characterization of LC-Fe_2O_3-NPs

2.4.1 Scanning Electron Microscope (SEM)

The SEM image of LC-Fe_2O_3-NPs indicate that the surface morphology of this sample has nanoparticles that appear to be spherical but have a wide size range, producing dense clusters as a result of agglomeration, which is presumably caused by magnetic interactions between Fe_2O_3 particles as shown in (Fig. 5).

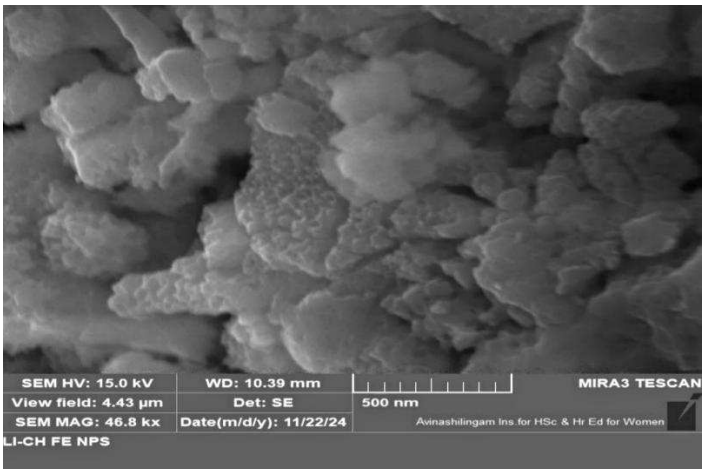


Fig.5. SEM image for LC-Fe_2O_3-NPs

2.4.2 X-ray Photoelectron Spectroscopy (XPS)

The primary components Fe, O, and C, which are characteristic of Iron Oxide nanoparticles made from plant extracts, are visible in the XPS spectrum of LC-Fe_2O_3 nanoparticles in (Fig. 6). The formation of Fe_2O_3 is confirmed by the Fe2p peaks in the binding energy range of 710-725 eV. Lattice oxygen connected to Fe-O bonding is shown by a significant O1s signal at about 530 eV. Peel extracts contain carbon-containing compounds and phytochemicals that operate as natural reducing and stabilizing agents during the formation of nanoparticles causing the C1s peak, which is located close to 285 eV.

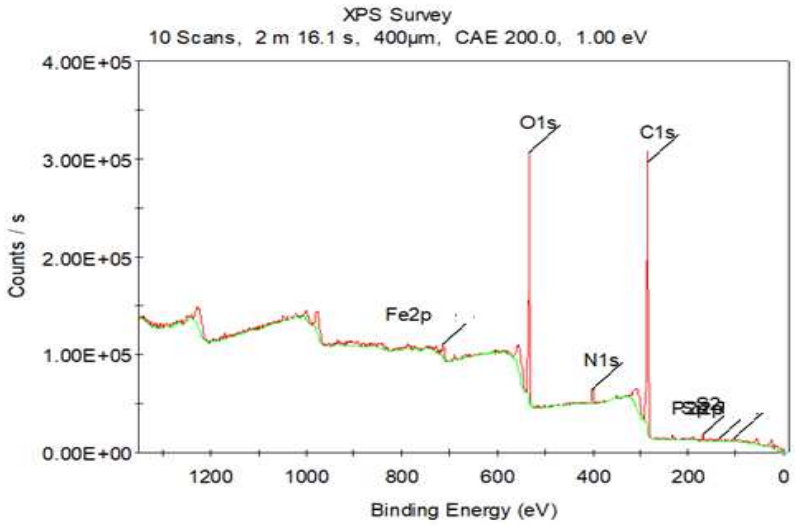


Fig. 6. XPS analysis for LC-Fe_2O_3-NPs.

2.4.3 X-ray Diffraction Analysis (XRD)

The crystalline structure of the produced nanoparticles is shown by the XRD pattern, which displays several distinct and broadened peaks. notable peaks of diffraction. The nanoscale crystallite sizes of the Fe_2O_3 particles are suggested by the observed peak widening. The exceptional purity of the biosynthesized nanoparticles is indicated by the lack of impurity peaks in the below (Fig. 7). Overall, the XRD examination confirms that crystalline Fe_2O_3 nanoparticles were successfully formed

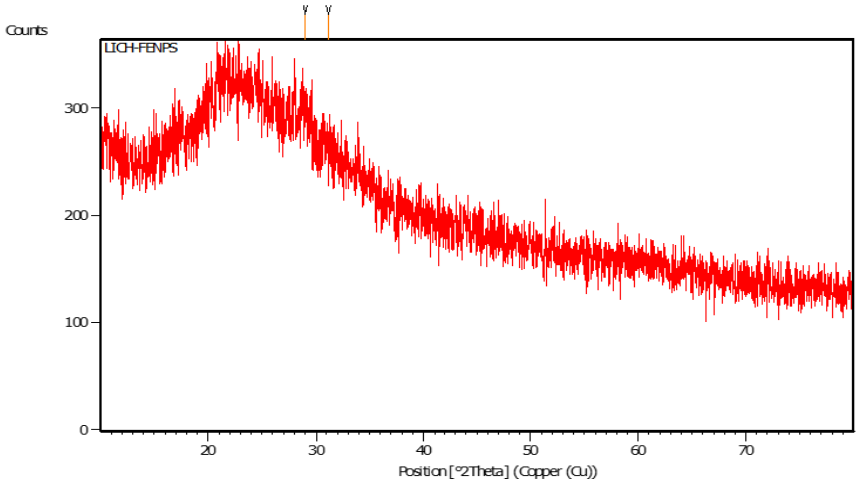


Fig. 7. XRD analysis for LC-Fe_2O_3-NPs.

2.4.4 Thermogravimetric Analysis (TGA)

The TGA curve for LC-Fe_2O_3-NPs (Fig. 8) reveals three distinct stages of weight loss, indicating thermal degradation features. The initial weight loss below 150 °C results from the evaporation of physically adsorbed water and moisture from the nanoparticle surface. The second major weight loss, which happens between 200 and 400 °C, is caused by the breakdown of organic compounds and phytochemicals present in Litchi chinensis peel extract, which was used as a reducing and stabilizing agent during synthesis. Beyond 450 °C, the removal of remaining organic matter and possible structural rearrangements within the Iron Oxide matrix result in a consistent and minor mass loss. The stable residual mass at higher temperatures promotes the formation of thermally stable Fe_2O_3 nanoparticles.

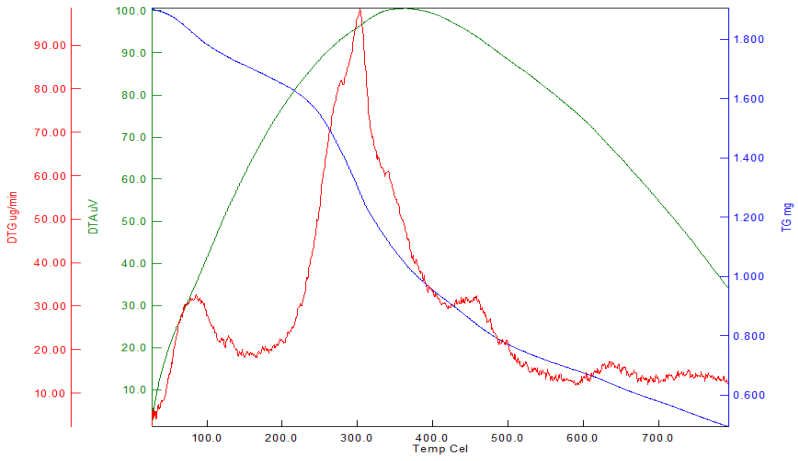


Fig. 8. TGA curve for LC-Fe_2O_3-NPs

2.4.5 Brunauer-Emmett-Teller (BET) Analysis

The LC-Fe_2O_3-NPs exhibit a moderate BET surface area of 17.957 m^2/g, which indicates low porosity. With a surface area of 29.060 m^2/g, a total pore volume of 0.199 cc/g, and a dominant pore diameter of about 2.014 nm, the BJH desorption investigation reveals a mesoporous structure that falls within the mesoporous range. At high relative pressures (P/P_2 >0.9), the nitrogen

adsorption-desorption isotherm displays a hysteresis loop, suggesting the existence of inter-particle gaps and slit-shaped pores. The creation of dense nanoparticle frameworks with limited internal porosity is supported by the reported sample density of 1.556 g/cc and the relatively small pore volume.

3. Results and Discussions

3.1 Adsorption of Congo Red and Alizarin Red S dye onto Litchi chinensis Peels of Iron Oxide nanoparticles (LC-Fe_2O_3-NPs)

Characterizing the adsorbent is crucial to understanding its properties. The effects of process variables, including temperature, agitation time, adsorbent dosage, solution pH and initial dye concentration were examined using batch studies. This section analyzes experimental findings from employing peels of Litchi chinensis -based Iron Oxide nanoparticles (LC-Fe_2O_3-NPs) as an adsorbent. The research involve equilibrium, kinetic, and thermodynamic evaluations aimed at understanding the mechanisms that drive dye adsorption. Furthermore, process conditions were optimized using response surface methods to determine the most effective parameters for increasing dye removal efficiency.

3.1.1 Effect of agitation time

The elimination rate is constant since after 30 minutes, both CR and ARS dye reached equilibrium. When the agitation period was extended from 5 to 30 minutes for an initial dye concentration of 20 mg/l, the dye removal percentage rise from 53.2% to 70% for CR Dye (Fig. 9) and from 62% to 77.5% for ARS dye in (Fig. 10).

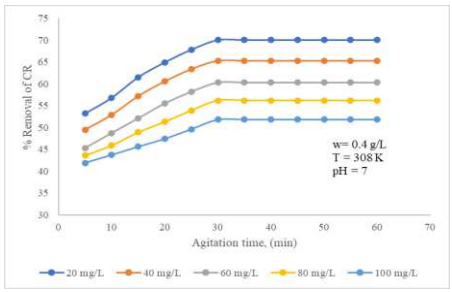


Fig. 9. Effect of agitation time on % dye removal of CR using LC-Fe_2O_3-NPs.

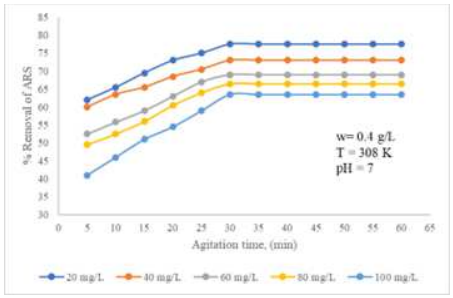
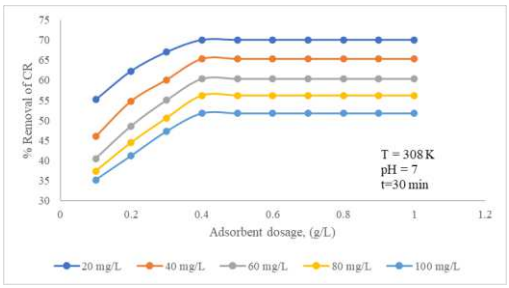


Fig. 10. Effect of agitation time on % dye removal of ARS using LC-Fe_2O_3-NPs.

3.1.2 Effect of adsorbent dosage

The results clearly demonstrate that higher adsorbent dosages increased the effectiveness of dye removal. Specifically, when the adsorbent dosage increased from 0.1 to 1.0 g/l for an initial dye concentration of 20 mg/l, the percentage of dye removed improved from 55.2% to 70% for CR dye and from 60.5% to 77.5% for ARS dye from (Fig. 11) and (Fig. 12).



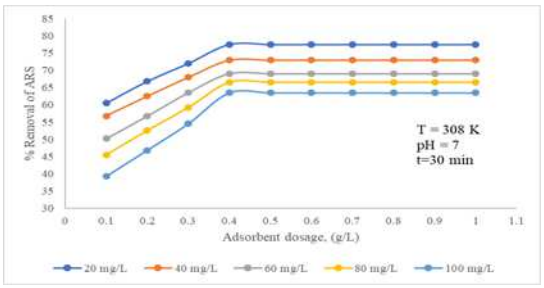


Fig. 11. Effect of adsorbent dosage on % dye removal of CR using LC-Fe_2O_3 NPs.

Fig. 12. Effect of adsorbent dosage on % dye removal of ARS using LC-Fe_2O_3-NPs.

3.1.3 Effect of solution pH

Shows that increasing the pH from 2 to 6 significantly improved dye removal efficiency for CR Dye from (Fig. 13); however, increasing the pH from 6 to 9 lowered it. The pH of the solution determines the adsorbent's surface charge, which is critical for adsorption. The percentage of dye removal for ARS Dye improved dramatically when the pH increased from 2 to 4 , but decreased when the pH increased from 4 to 9 as shown in (Fig. 14). The decrease in adsorption at pH 4 indicates that the interaction between LC-Fe_2O_3-NPs and ARS Dye is not simply governed by electrostatic attraction.

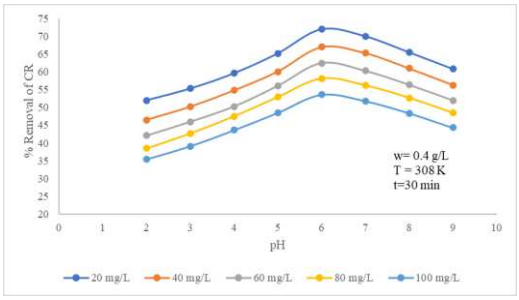


Fig. 13. Effect of solution pH on % dye removal of CR using LC-Fe_2O_3-NPs.

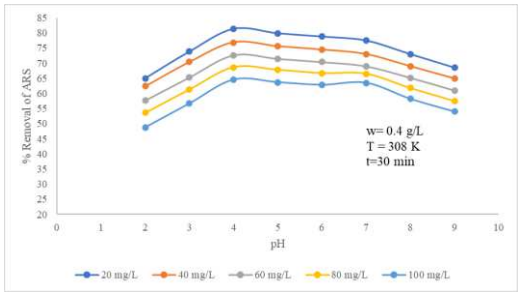


Fig. 14. Effect of solution pH on % dye removal of ARS using LC-Fe_2O_3-NPs.

3.1.4 Effect of initial concentration of dye

When the starting dye concentration was increased from 10 to 100 mg/L, the percentage of dye removal from 95.62% to 68.49% in CR Dye and from 96% to 74.66% in ARS Dye. This decline indicates that rising dye concentrations cause saturation of the available active sites on the adsorbent surface. Furthermore, the data demonstrate that increasing the initial dye concentration from 10 to 100 mg/L enhances adsorption capacity from 23.9 to 171.23 mg/g for CR Dye (Fig. 15) and 24 to 186.66 mg/g for ARS Dye (Fig. 16).

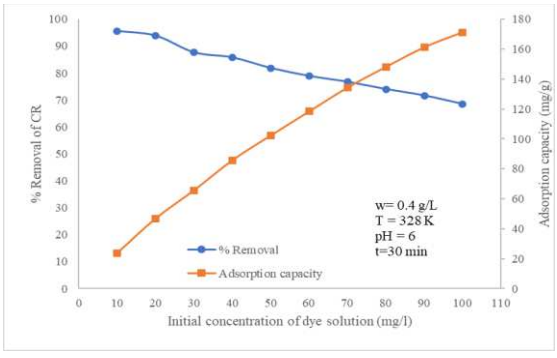


Fig. 15. Effect of initial dye solution on adsorption capacity and % dye removal of CR using LC-Fe_2O_3-NPs.

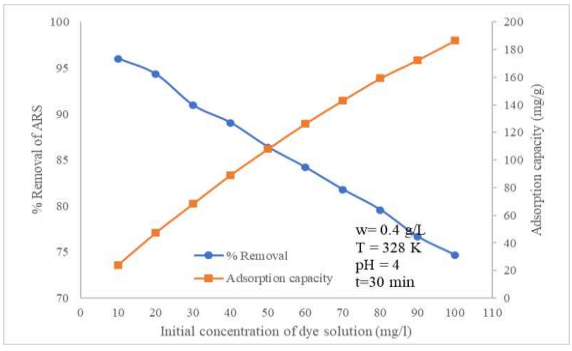


Fig. 16. Effect of initial dye concentration on adsorption capacity on % dye removal of ARS using LC-Fe_2O_3-NPs.

3.1.5 Effect of temperature

The effect of temperature on CR dye and ARS dye adsorption was investigated from 308 to 328 K. At a starting dose of 20 mg/l, dye removal for CR increased from 70% to 93.8%, while ARS increased from 81.4% to 94.3% as temperature increase from (Fig. 17) and (Fig. 18). This pattern indicates the adsorption process is endothermic.

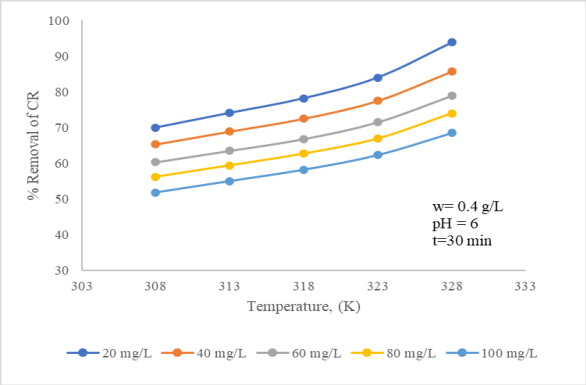


Fig. 17. Effect of temperature on % dye removal of CR using LC-Fe_2O_3-NPs.

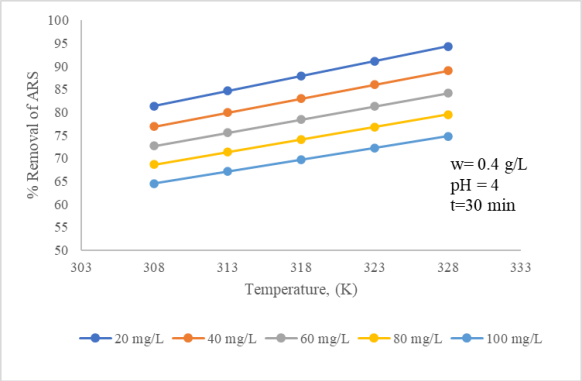


Fig. 18. Effect of temperature on % dye removal of ARS using LC-Fe_2O_3-NPs.

3.2 Equilibrium studies

3.2.1 Langmuir adsorption isotherm

The Langmuir isotherm model is presented by the following (Eq. 1)

$$q_e = \frac{k_L q_{max} C_e}{1+bC_e} \quad (1)$$

where q_{max} (mg/g) is the Langmuir constant associated with the maximum monolayer adsorption capacity, k_L (L/mg) is the constant associated with the free energy or net enthalpy of adsorption, C_e (mg/L) is the equilibrium dye ion concentration in the solution, and q_e (mg/g) is the amount of dye adsorbed per unit mass of adsorbent.

The Langmuir model in linear form is given as (Eq. 2)

$$\frac{C_e}{q_e} = \frac{1}{k_L q_{max}} + \frac{1}{q_{max}} C_e \quad (2)$$

(Fig. 19) and (Fig. 20) display the Langmuir plots (C_e/q_e versus C_e) for the adsorption of Congo Red and Alizarin Red S dyes at a temperature of 328 K, respectively.

Langmuir isotherm constants and correlation coefficients values are listed in (Table 1).

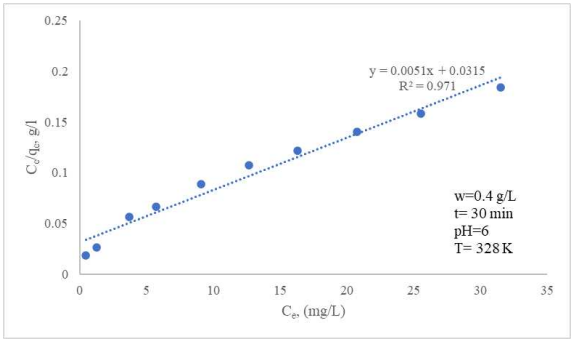


Fig. 19. Langmuir isotherm for adsorption of CR dye onto LC-Fe_2O_3-NPs.

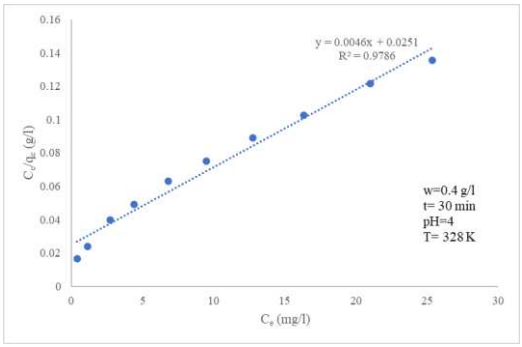


Fig. 20. Langmuir isotherm for adsorption of ARS dye onto LC-Fe_2O_3-NPs.

3.2.2 Freundlich isotherm

This Freundlich isotherm model is given as (Eq. 3)

$$q_e = K_f C_e^{1/n} \quad (3)$$

where C_e is the equilibrium concentration (mg/l), q_e is the quantity of dye adsorbed per unit mass of adsorbent at equilibrium (mg/g), K_f is the Freundlich adsorption constant associated with the adsorbent's adsorption capacity (mg/g)/(L/g)n), and 1/n is a dimensionless constant.

The linear form of Freundlich isotherm as given in (Eq. 4)

$$lnq_e = lnK_f + \frac{1}{n} lnC_e \quad (4)$$

(Fig. 21) and (Fig. 22) displays the Freundlich Plots (ln q_e versus ln C_e) for the adsorption of CR Dye and ARS dye at 328K . Freundlich isotherm constants and correlation coefficients values are listed in (Table 1).

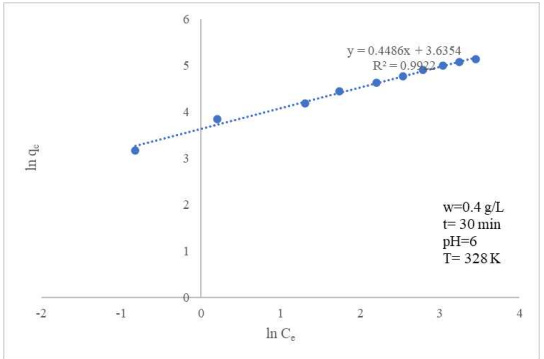


Fig. 21. Freundlich isotherm for adsorption of CR dye onto LC-Fe_2O_3-NPs adsorbent.

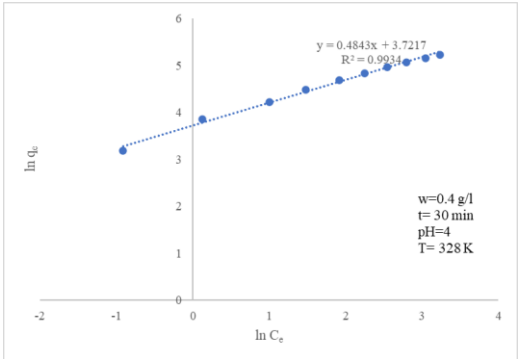


Fig. 22. Freundlich isotherm for adsorption of ARS dye onto LC-Fe_2O_3-NPs adsorbent.

3.2.3 Temkin isotherm

The equation for the Temkin isotherm is expressed as (Eq. 5)

$$q_e = \frac{RT}{b} \ln (A_T C_e) \quad (5)$$

The linear form of Temkin equation is given (Eq. 6)

$$q_e = B_T ln A_T + B_T ln C_e \quad (6)$$

where A_T is the equilibrium binding constant (Lg^{-1}), $B_T = RT/b$, R is the universal gas constant (8.314 $Jmol^{-1}K^{-1}$), b is related to the heat of adsorption (J mol-1), T is the absolute temperature (K), and q_e (mg/g) and C_e (mg/L) are the amounts of adsorbed dye per unit weight of adsorbent and un-adsorbed dye concentration in solution at equilibrium, respectively.

(Figs. 23 and 24) show the linear plot of q_e versus ln C_e for CR and ARS Dyes adsorption onto the adsorbent and the values of the parameters are given in (Table 1).

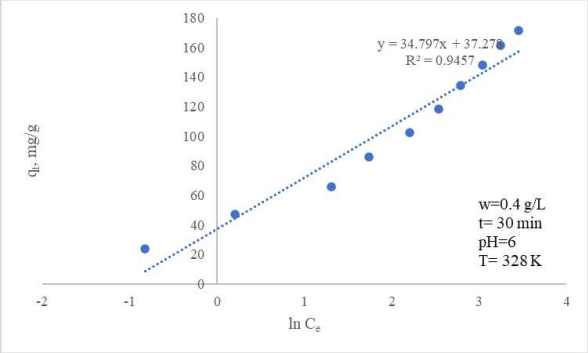


Fig. 23. Temkin isotherm for adsorption of CR dye onto LC-Fe_2O_3-NPs adsorbent.

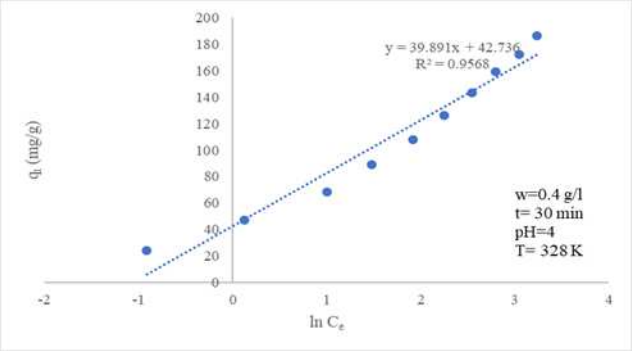


Fig. 24. Temkin isotherm for adsorption of ARS dye onto LC-Fe_2O_3-NPs adsorbent.

Table 1. Adsorption isotherm constants for removal of Congo Red (CR) and Alizarin Red S (ARS) dyes using LC-Fe_2O_3-NPs as adsorbent.

Isotherm model	Constants	CR dye	ARS dye
Langmuir	k_L (L/mg)	0.162	0.183
	q_{max} (mg/g)	196.07	217.39
	R_L	0.0855	0.0769
	R^2	0.97	0.9786
Freundlich	k_F ($mg^{1-1/n}L^{1/1}g^{-1}$)	37.17	41.26
	1/n	0.448	0.484
	R^2	0.9922	0.9932
Temkin	A_T (lg^{-1})	1.588	2.918
	B_T ($J\ mol^{-1}$)	34.797	39.891
	R^2	0.9457	0.9568

3.3 Kinetic studies

3.3.1 Pseudo-first order model

The pseudo first order kinetic equation is (Eq. 7)

$$\frac{dq_t}{dt} = k_1(q_e - q_t) \quad (7)$$

where t is the agitation time (min), k1 is the equilibrium rate constant of pseudo-first-order sorption (min^{-1}), qt is the amount of dye adsorbed at time t (mg/g), and qe is the adsorption capacity in equilibrium (mg/g).

After definite integration by applying the initial conditions q_t =0 at t =0 and q_t = q_t and t=t the equation becomes, (Eq. 8)

$$ln(q_e - q_t) = lnq_e - k_1 t \quad (8)$$

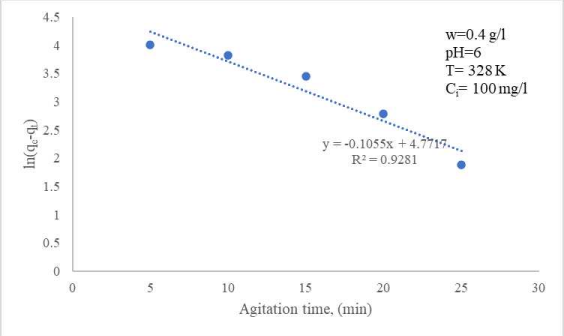


Fig. 25. Pseudo first order kinetics for adsorption of CR dye onto LC-Fe_2O_3-NPs adsorbent.

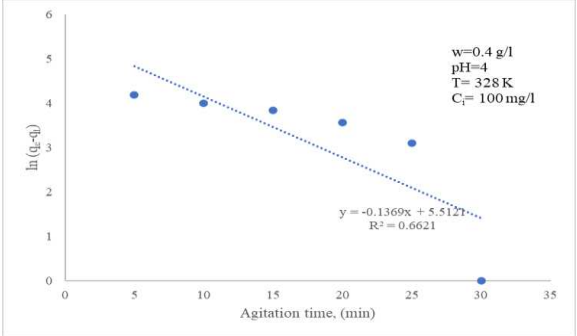


Fig. 26. Pseudo first order kinetics for adsorption of ARS dye onto LC-Fe_2O_3-NPs adsorbent.

The linear plots for the pseudo-first order model is presented in (Fig. 25) and (Fig. 26). From these plots, the intercept and slope were used to calculate the equilibrium adsorption capacity and the first-order rate constant, which are summarized along with the correlation coefficients (R^2) for CR and ARS dyes in (Tables 2 and 3), respectively.

3.3.2 Pseudo-second order model:

The pseudo second order equation is expressed in the form (Eq. 9)

$$\frac{dq}{dt} = k_2[q_e - q_t]^2 \quad (9)$$

Where, q_t is the amount of dye adsorbed at time t (mg/g); q_e is the adsorption capacity at equilibrium (mg/g); k_2 is the equilibrium rate constant of pseudo-second-order sorption (g/mol-min); and t is the time (min).

After definite integration by applying the initial conditions q = 0 at t = 0 and q = q_t at t= t, the equation becomes, (Eq. 10)

$$\frac{t}{q_t} = \frac{1}{k_2 q_e^2} + \frac{1}{q_e} t \quad (10)$$

Plots of t/q_t (g.min/mg) versus t (min) were employed to evaluate the applicability of the pseudo-second order kinetic model for the adsorption of Congo Red and Alizarin Red S dyes onto LC-Fe_2O_3-NPs individually. (Fig. 27) and (Fig. 28) display these plots. The slope and intercept of the linear plots provide the values for the equilibrium adsorption capacity (q_e) and the second-order rate constant, which are detailed in (Tables 2 and 3).

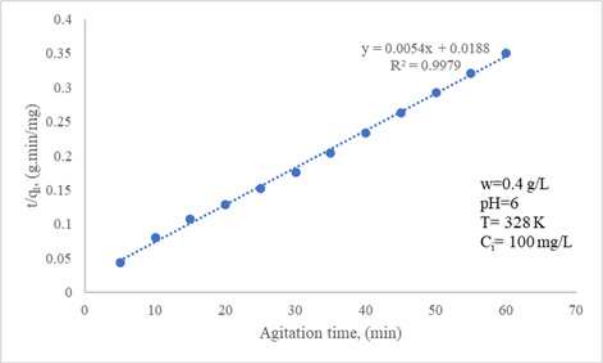


Fig. 27. Pseudo second order kinetics for adsorption of CR dye onto LC-Fe_2O_3-NPs adsorbent.

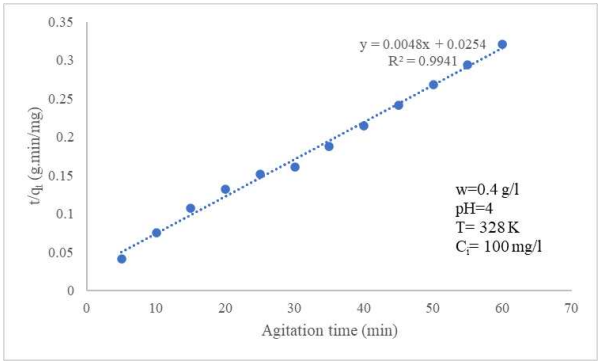


Fig. 28. Pseudo second order kinetics for adsorption ARS dye onto LC-Fe_2O_3-NPs adsorbent.

3.3.3 Elovich model

The Elovich model describes the type of adsorption mechanism (physical and chemical). It is expressed as (Eq. 11)

$$\frac{dq}{dt} = \alpha e^{-\gamma q} \tag{11}$$

Where α is the initial rate and γ is the extent of surface covering and activation energy required for chemisorption (g/mg). Integrating the following equation between the boundary conditions q=0 at t=0 and q = q at t=t yields. Where $t_0 = 1/\ \alpha\ \gamma$. Simplifying the above equation under very large t over t_0, gives (Eq. 12)

$$q = \frac{1}{\gamma}\ln(\alpha\gamma) + \frac{1}{\gamma}\ln t \tag{12}$$

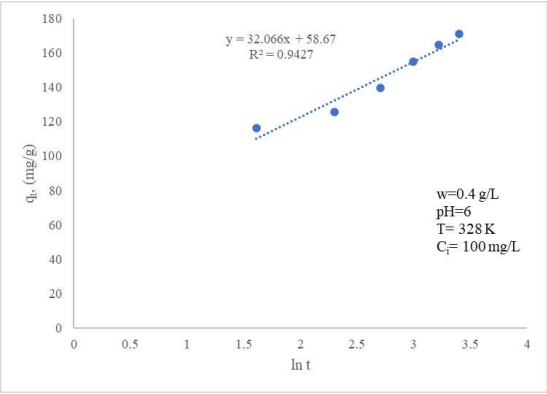


Fig. 29. Elovich model for adsorption of CR dye onto LC-Fe_2O_3-NPs adsorbent.

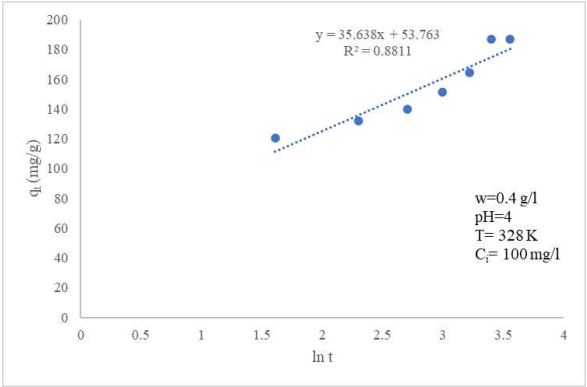


Fig. 30. Elovich model for adsorption of ARS dye onto LC-Fe_2O_3-NPs adsorbent.

The constants are obtained from the slope and intercept of a straight-line plot of q vs ln t shown in (Figs. 29 and 30).

The Elovich equation data obtained in this study for the adsorption of CR and ARS dyes onto LC-Fe_2O_3-NPs adsorbent is summarized in (Tables 2 and 3) respectively.

3.3.4 Intra particle diffusion model

The Weber-Morris intra particle diffusion model is expressed as (Eq. 13)

$$q = K_{id} t^{1/2} + I \tag{13}$$

where q is the amount of dye adsorbed at time t, K_{id} is the intra particle diffusion rate constant ($mg.g^{-1}.min^{-1/2}$), and I is the thickness of the boundary layer. The higher the value of I, the greater the contribution of surface sorption in the rate-controlling step.

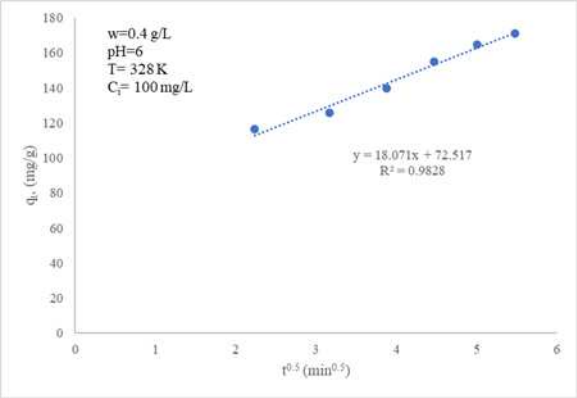


Fig. 31. Intra particle diffusion model for adsorption of CR dye onto LC-Fe_2O_3 NPs adsorbent.

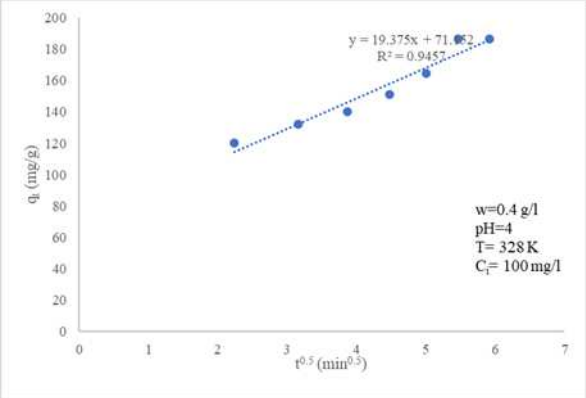


Fig. 32. Intra particle diffusion model for adsorption of ARS dye onto LC-Fe_2O_3-NPs adsorbent.

The intra-particle diffusion rate constants (K_{id}) for CR and ARS dyes were calculated and are presented in (Tables 2 and 3), respectively. (Fig. 31) and (Fig. 32) display the plots of the intra-particle diffusion model.

The linear regions in these plots do not pass through the origin, indicating that intra-particle diffusion is not the sole rate-limiting step in the adsorption process. Additionally, the high intercept values suggest that the boundary layer effect significantly influences the overall adsorption kinetics, contributing to the rate control alongside intra-particle diffusion.

Table 2. Kinetic model parameters for CR dye removal using LC-Fe_2O_3-NPs

Concentration, mg/l	Pseudo first order kinetics		
	k_1 (1/min)	q_e (mg/g)	R^2
100	0.1055	117.91	0.9281
	Pseudo second order kinetics		
	k_2 (g/mg.min)	$q_{e,cal}$ (mg/g)	R^2
	0.00155	185.18	0.9979
	Elovich model		
	γ (g/mg)	α (mg/g.in)	R^2
	0.0311	82.5	0.9427
	Intra particle diffusion model		
	K_{id1}, $mg.g.min^{1/2}$	I_1, mg/g	R^2
	18.071	72.517	0.9828

Table 3. Kinetic model parameters for ARS dye removal using LC-Fe_2O_3-NPs

Concentration, mg/l	Pseudo first order kinetics		
	k_1 (1/min)	q_e (mg/g)	R^2
100	0.1369	247.64	0.6621
	Pseudo second order kinetics		
	k_2 (g/mg.min)	$q_{e,cal}$ (mg/g)	R^2
	0.000907	208.31	0.9941
	Elovich model		
	γ (g/mg)	α (mg/g.min)	R^2
	0.028	160.83	0.8811
	Intra-particle diffusion model		
	K_{id1}, mg/g.$min^{1/2}$	I_1, mg/g	R^2
	19.375	71.15	0.9457

3.4 Thermodynamic studies

The relationship between the standard free energy change and the equilibrium constant is expressed by the following (Eq. 14)

$$\Delta G° = -RTlnK_c \quad (14)$$

where R is the universal gas constant, T is the temperature (K) and K_c value was calculated using the following (Eq. 15),

$$K_c = \frac{q_e}{C_e} \quad (15)$$

Where q_e is the dye uptake and C_e is the equilibrium adsorbate concentration in solution.

The enthalpy changes ΔH° and entropy change ΔS° of the adsorption were estimated from the following (Eq. 16),

$$lnK_c = \frac{\Delta S°}{R} - \frac{\Delta H°}{RT} \quad (16)$$

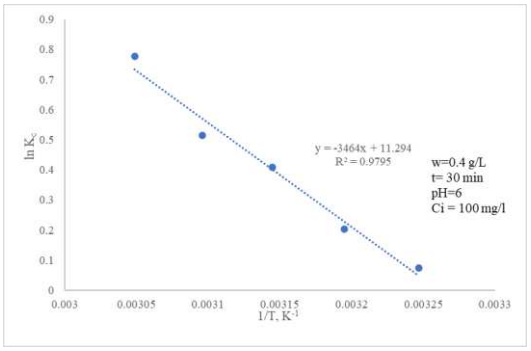


Fig. 33. Thermodynamics studies for adsorption of CR dye onto LC-Fe_2O_3-NPs adsorbent.

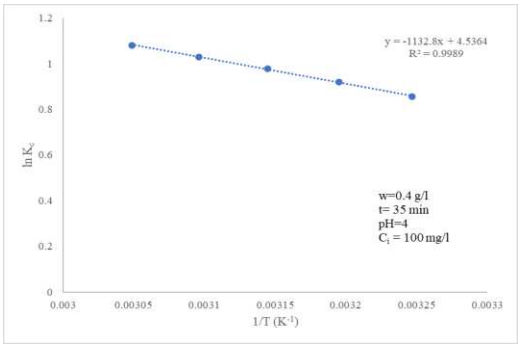


Fig. 34. Thermodynamics studies for adsorption of ARS dye onto LC-Fe_2O_3-NPs adsorbent.

The ΔH° and ΔS° values were obtained from the slope and intercept of the Van 't Hoff plots (Figs. 33 and 34), with results summarized in (Table 4). The correlation coefficients (R^2) were 0.9795 for CR and 0.9989 for ARS, indicating excellent linearity.

The negative ΔG° values across the temperature range confirm the spontaneous nature of the adsorption, demonstrating its feasibility. The decreasing trend of ΔG° with increasing temperature suggests that adsorption becomes less spontaneous at higher temperatures.

The positive ΔH° value indicates that the process is endothermic, meaning that more energy is required to break bonds than is released during the formation of adsorbed complexes. The positive ΔS° implies that there is little change in the internal structure of the adsorbent during adsorption, which is consistent with minimal structural rearrangement of LC-Fe_2O_3-NPs during the dye adsorption process.

Table 4. Thermodynamic parameters for CR and ARS dyes adsorption using LC-Fe_2O_3-NPs adsorbent.

Temperature, K	CR dye			ARS dye		
	ΔG° (kJ/mol)	ΔH° (kJ/mol)	ΔS° (J/mol K)	ΔG° (kJ/mol)	ΔH° (kJ/mol)	ΔS° (J/mol K)
308	-18.86	28.79	98.89	-21.90	94.18	37.71
313	-52.93			-23.93		
318	-10.77			-25.85		
323	-13.82			-27.62		
328	-21.17			-29.47		

3.5 Characterization of Peels of *Litchi chinensis*-Iron Oxide Nanoparticles (LC-Fe_2O_3-NPs) using FTIR analysis

3.5.1 Fourier Transform Infrared Spectroscopy (FTIR) for LC-Fe_2O_3-NPs before adsorption

From (Fig. 35), the spectrum of LC-Fe_2O_3-NPs displays broad absorption bands in the range of 3000–3800 cm^{-1}, which correspond to O–H stretching vibrations from hydroxyl groups and adsorbed water molecules. Additionally, peaks around 1620–1630 cm^{-1} are observed, attributed to C=O stretching of carboxyl groups and aromatic C=C stretching associated with phytochemicals such as flavonoids and terpenoids present in the extract. Most of the bands in the spectra are characteristic of these phytochemicals, indicating their presence on the nanoparticle surface. A low-intensity band near 1023 cm^{-1} corresponds to C=C stretching vibrations.

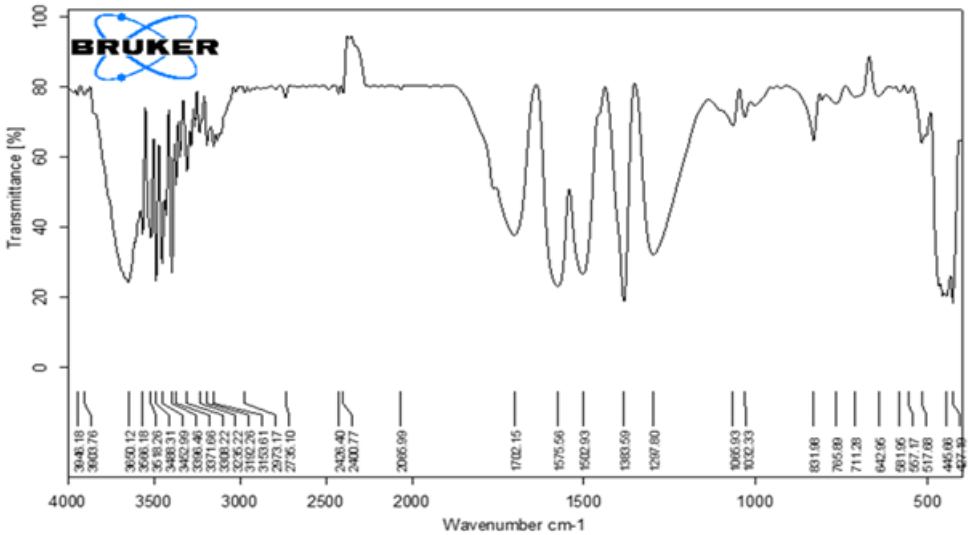


Fig. 35. FTIR spectra of peels of Litchi chinensis Iron Oxide nanoparticles before adsorption.

3.5.2 Fourier Transform Infrared Spectroscopy for LC-Fe_2O_3-NPs after adsorption with Congo Red dye

After adsorption of CR dye, the FTIR spectrum (Fig. 36) exhibits slight broadening and changes in peak intensity, suggesting hydrogen bonding interactions between hydroxyl groups on the nanoparticle surface and dye molecules. Notably, new peaks emerge at approximately 1702 cm^{-1}, and there is increased intensity around 1575 cm^{-1}. These spectral changes are characteristic of the azo (-N=N-) groups and aromatic structures within CR dye, confirming successful dye adsorption. The peak at 1702 cm^{-1} suggests the presence of sulfonic acid functional groups originating from the dye molecule. These observations indicate that the functional groups on the adsorbent surface, such as hydroxyl, carboxyl, and possibly sulfonic acid groups, play a crucial role in binding dye molecules. This evidence supports the conclusion that LC-Fe_2O_3-NPs are effective for the removal of CR from aqueous solutions.

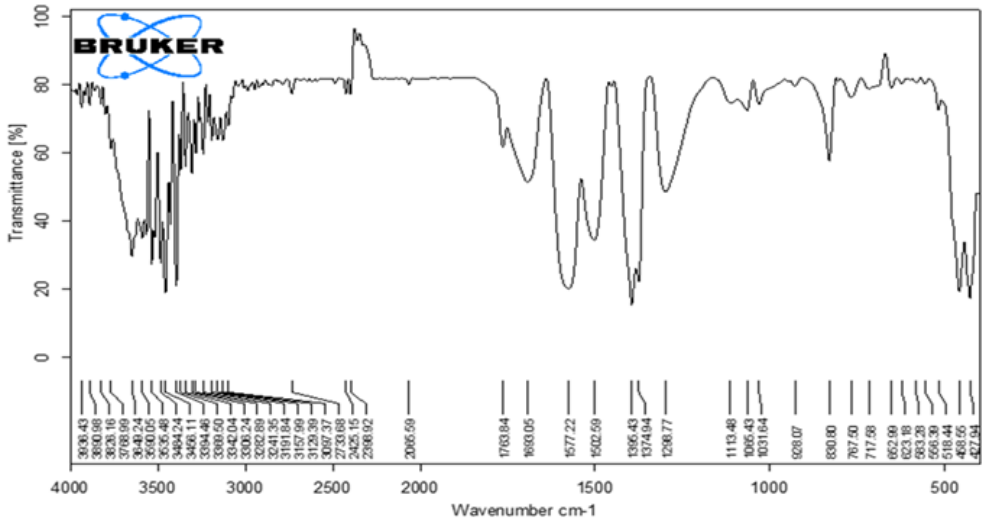


Fig. 36. Fourier Transform Infrared Spectroscopy (FTIR) for LC-Fe_2O_3-NPs after adsorption with CR dye

3.5.3 Fourier Transform Infrared Spectroscopy for LC-Fe_2O_3-NPs after adsorption with Alizarin Red S dye

Similarly, the FTIR spectrum of LC-Fe_2O_3-NPs after adsorption of Alizarin Red S (ARS) is shown in (Fig. 37). Post-adsorption, these spectra exhibit significant broadening and increased intensity, especially in the 3000–3600 cm^{-1} region, indicating extensive hydrogen bonding interactions between the hydroxyl groups of ARS, an anthraquinone derivative with multiple OH groups, and the nanoparticle surface. This suggests a stronger interaction compared to CR. New prominent peaks appear at approximately 1612 cm^{-1} and 1640 cm^{-1}, which are characteristic of C=O stretching vibrations from the quinone structure of ARS. Additional peaks around 1490 cm^{-1} and 1540 cm^{-1} correspond to aromatic C=C stretching vibrations from the anthracene backbone of the dye. These spectral features confirm that functional groups present on the adsorbent facilitate effective attachment of ARS molecules onto the surface. Overall, the data demonstrate that LC-Fe_2O_3-NPs are suitable and effective for the removal of ARS from aqueous solutions.

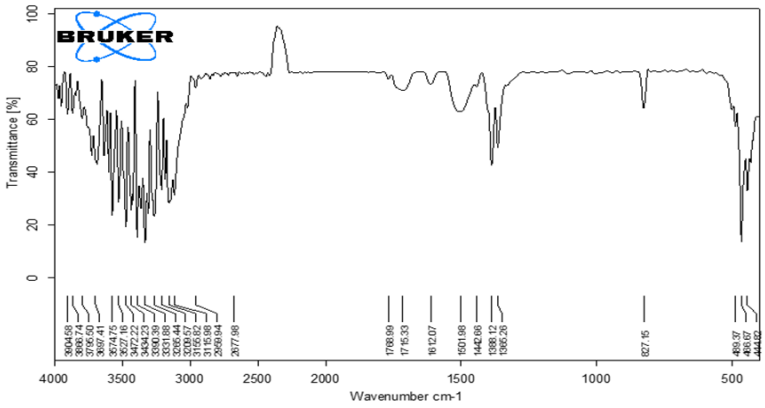


Fig. 37. Fourier Transform Infrared Spectroscopy (FTIR) for LC-Fe_2O_3-NPs after adsorption with ARS dye.

3.6 Optimization of adsorption process parameters using Response Surface Methodology (RSM)

Preliminary experimental data indicates that four factors significantly affect the percentage of dye removal using peels of (LC-Fe_2O_3-NPs): starting dye concentration, solution pH, adsorbent dosage, and temperature. In order to properly determine the ideal circumstances for obtaining the highest dye removal efficiencies for CR and ARS using RSM, these parameters were selected for further analysis.

A (BBD), which methodically looks at the effects and interactions among the parameters, was used in this study to analyze the impact of the selected variables. The percentage of dye removed (CR and ARS) by LC-Fe_2O_3-NPs is the response variable. The BBD offered a strong foundation for figuring out the ideal dye process parameters and consisted of 29 tests, including 16 cube points, 5 center points, and 8 axial points.

3.6.1 Optimization using Box Behnken Design (BBD)

In this investigation, a quadratic model was used to characterize the relationship between the response (% dye removal) and the process parameters. The regression equations for the removal of CR and ARS are defined by the functions of pH (A), equilibrium constant (K, B), initial dye concentration (C_i, C), and adsorbent dosage (w, D).

Table 5. Levels of different process variables for optimization using BBD for the adsorption of CR and ARS dyes onto LC-Fe_2O_3-NPs adsorbent.

Variable Name		Range and levels for CR dye			Range and levels for ARS dye		
		-1	0	+1	-1	0	+1
A	**Solution pH**	5	6	7	3	4	5
B	**Temperature T, K**	323	328	333	318	328	333
C	**Initial dye Concentration, C_i, mg/l**	10	20	30	10	20	30
D	**Adsorbent dosage w, g/L**	0.5	0.4	0.6	0.5	0.4	0.6

Equation in terms of coded factors for Congo Red dye

Removal of CR dye = +93.80+0.0417A -0.5583B-1.32C-0.2333D+0.5250AB-0.0250AC0.1750AD-0.1000BC+0.1500 BD +0.0250CD -4.34A^2-4.81B^2 -6.95C^2 -5.50D^2 (17)

Equation in terms of coded factors for Alizarin red S dye:

Removal of ARS dye=+94.3+0.0417A-0.4583B-2.32C-0.6333D+0.5550AB-0.0250AC0.1550AD-0.1210BC+0.1210BD +0.0250CD -4.28A²-5.54B² -6.45C² -4.80D² (18)

The predicted values for % dye removal of CR and ARS, based on the regression equations described earlier, are presented in (Table 6), alongside the corresponding experimental data. The regression coefficients for these models are detailed in (Table 7 and 8) for CR and ARS, respectively.

The model's goodness of fit is reflected in the regression coefficient (R^2), which was 0.9533 for CR and 0.9672 for ARS, indicating that a large proportion of variability in dye removal is explained by the model. P-values below 0.05 confirm that the models are statistically significant at the 95% confidence level. Furthermore, the P-values, Fisher's F-test values, and R^2 provide insights into how well the experimental process variables and their interactions predict the response variability. A reliable model should predict responses with reasonable accuracy, which is corroborated by the consistent alignment between predicted and experimental values (shown in Figs. 38 and 39).

Table 6. Experimental design matrix along with % dye removal of CR and ARS onto LC-Fe_2O_3-NPs adsorbent.

Run no.	A, pH	B, T	C, Ci	D, w	% dye removal of CR dye		A, pH	B, T	C, Ci	D, w	% dye removal of ARS dye	
					Experimental	Predicted					Experimental	Predicted
1.	6	333	10	0.5	79.5	80.50	4	328	10	0.4	86.5	87.00
2.	6	333	30	0.5	77.4	77.66	3	323	10	0.4	87.6	87.54
3.	6	328	30	0.4	76.9	77.84	4	318	20	0.3	87.2	87.26
4.	6	328	20	0.4	93.8	93.8	5	323	20	0.3	87.5	87.92
5.	7	323	20	0.5	82.5	82.33	4	328	20	0.5	87.9	87.90
6.	6	328	20	0.4	93.8	93.8	3	323	20	0.3	87.8	88.04
7.	6	323	20	0.6	81.6	81.26	4	323	20	0.4	94.3	94.3
8.	6	328	30	0.6	77.2	77.43	4	328	20	0.3	87.8	87.85
9.	6	323	10	0.5	80.2	81.41	4	318	20	0.5	87.6	87.61
10.	5	328	20	0.4	80.5	81.58	4	323	20	0.4	94.3	94.3
11.	7	333	20	0.5	81.5	82.26	3	323	20	0.5	88.1	88.54
12.	6	328	10	0.4	79.6	80.53	5	323	20	0.5	87.2	87.82
13.	6	333	20	0.4	82.9	80.61	4	323	20	0.4	94.3	94.3
14.	6	328	10	0.6	79.8	80.01	5	323	30	0.4	86.2	86.32
15.	6	328	20	0.4	93.8	93.85	3	328	20	0.4	88.5	88.17
16.	5	328	10	0.5	83.4	81.36	5	323	10	0.4	87.2	87.07
17.	7	328	30	0.5	79.4	78.81	4	323	10	0.3	87.6	87.19
18.	5	323	20	0.5	82.9	83.29	3	323	30	0.4	86.5	86.69
19.	6	323	20	0.4	83.6	82.03	4	318	30	0.4	85.4	85.76
20.	5	328	30	0.5	80.1	78.78	4	323	30	0.3	86.6	86.24
21.	6	328	20	0.4	93.8	93.85	4	323	20	0.4	94.3	94.3
22.	5	328	20	0.6	80.9	81.46	5	328	20	0.4	88.2	87.77
23.	6	328	20	0.4	93.8	93.8	4	323	10	0.5	87.8	87.24
24.	6	333	20	0.6	81.5	80.45	4	328	30	0.4	86.2	86.40
25.	5	333	20	0.5	79.8	81.13	5	318	20	0.4	87.9	87.31
26.	7	328	20	0.6	80.8	81.20	4	323	20	0.4	94.3	94.3
27.	7	328	20	0.4	81.1	82.01	4	323	30	0.5	87.1	86.59
28.	7	328	10	0.5	82.8	81.50	4	318	10	0.4	86.1	86.76
29.	6	323	30	0.5	78.5	78.98	3	318	20	0.4	88.23	87.74

Table 7. ANOVA table for model to predict % removal of CR onto LC-Fe_2O_3-NPs adsorbent using BBD

Source	Sum of Squares	Df	Mean Square	F-value	p-value
Model	540.32	14	38.59	20.43	< 0.0001
A-pH	0.0208	1	0.0208	0.0110	0.9179
B-Temperature	3.74	1	3.74	1.98	0.1812
C-Initial concentration	20.80	1	20.80	11.01	0.0051
D-Adsorbent dosage	0.6533	1	0.6533	0.3458	0.5659
AB	1.10	1	1.10	0.5836	0.4576
AC	0.0025	1	0.0025	0.0013	0.9715
AD	0.1225	1	0.1225	0.0648	0.8027
BC	0.0400	1	0.0400	0.0212	0.8864
BD	0.0900	1	0.0900	0.0476	0.8304
CD	0.0025	1	0.0025	0.0013	0.9715
A^2	122.04	1	122.04	64.60	< 0.0001
B^2	150.23	1	150.23	79.52	< 0.0001
C^2	313.31	1	313.31	165.84	< 0.0001
D^2	196.22	1	196.22	103.86	< 0.0001
Residual	26.45	14	1.89		
Lack of Fit	26.45	10	2.64		
Pure Error	0.0000	4	0.0000		
Cor Total	566.77	28			

df- degree of freedom; SS- the sum of squares; F- factor F; P- probability

Table 8. ANOVA table for model to predict % removal of Alizarin Red S onto LC-Fe_2O_3-NPs adsorbent using BBD

Source	Sum of Squares	Df	Mean Square	F-value	p-value
Model	103.50	14	7.39	29.52	< 0.0001
A-pH	0.5334	1	0.5334	2.13	0.1665
B-Temperature	0.5941	1	0.5941	2.37	0.1458
C-Initial concentration	1.92	1	1.92	7.67	0.0151
D-Adsorbent dosage	0.1200	1	0.1200	0.4791	0.5001
AB	0.0002	1	0.0002	0.0009	0.9765
AC	0.0025	1	0.0025	0.0100	0.9218
AD	0.0900	1	0.0900	0.3593	0.5584
BC	0.0400	1	0.0400	0.1597	0.6955
BD	0.0225	1	0.0225	0.0898	0.7688
CD	0.0225	1	0.0225	0.0898	0.7688
A^2	23.77	1	23.77	94.89	< 0.0001
B^2	35.49	1	35.49	141.71	< 0.0001
C^2	65.61	1	65.61	261.97	< 0.0001
D^2	26.09	1	26.09	104.16	< 0.0001
Residual	3.51	14	0.2505		
Lack of Fit	3.51	10	0.3506		
Pure Error	0.0000	4	0.0000		
Cor Total	107.01	28			

df- degree of freedom; SS- the sum of squares; F-factor F; P- probability

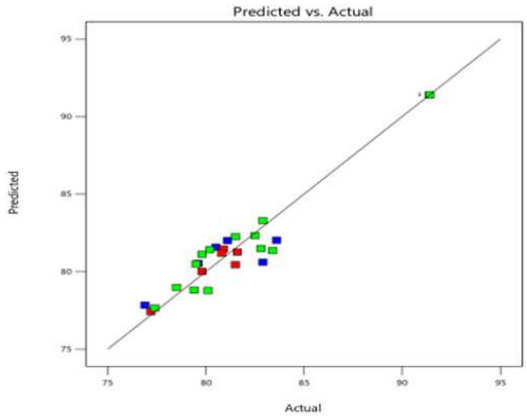


Fig. 38. Predicted values vs actual values from BBD for CR (Parity plot).

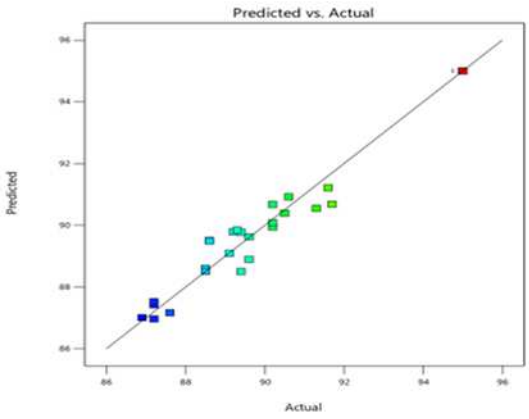


Fig. 39. Predicted values vs. actual values from BBD for ARS (Parity plot).

3.6.2 Interaction effects of adsorption variables

When the temperature and adsorbent dosage are kept at their mid-values, the CR and ARS dyes response surface curves demonstrate the interaction between the initial dye concentration and solution pH. Comparable response surface graphics show how temperature and adsorbent dose interact to influence dye removal efficiency. Overall, the data indicates that dye removal percentages increase with increased adsorbent dosage and temperature, although dye concentration and solution pH tend to reduce removal efficiency. The connection between the initial dye concentration and pH of the solution while the adsorbent dosage and temperature are maintained at their mid-values. Similar response surface plots show how the interaction between temperature and adsorbent dosage influences dye removal efficacy. Overall, the data indicates that dye removal percentages increase with higher adsorbent dosage and temperature, whereas increasing dye concentration and solution pH tends to decrease removal efficiency. Response surface curves for CR dye are displayed from (Fig. 40-51).

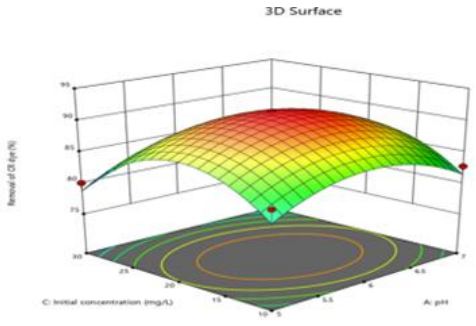


Fig. 40. Response surface plot of initial concentration vs solution pH on % dye removal of CR.

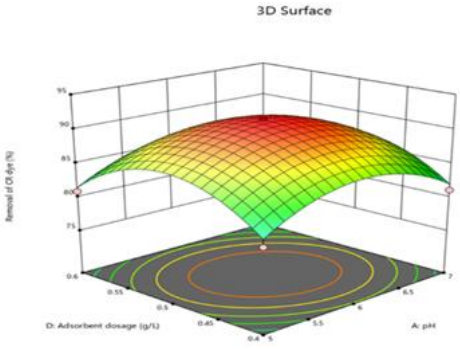


Fig. 41. Response surface plot of adsorbent dosage vs solution pH on % dye removal of CR.

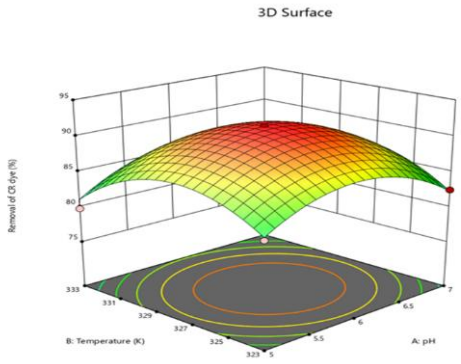


Fig. 42. Response surface plot of temperature vs Solution pH on % dye removal of CR.

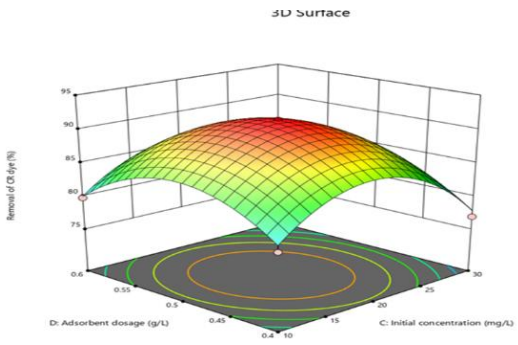


Fig. 43. Response surface plot of initial concentration vs absorbent dosage on % dye removal of CR.

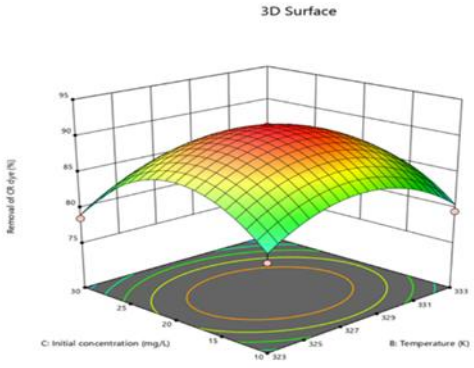


Fig. 44. Response surface plot of initial concentration vs temperature on % dye removal of CR.

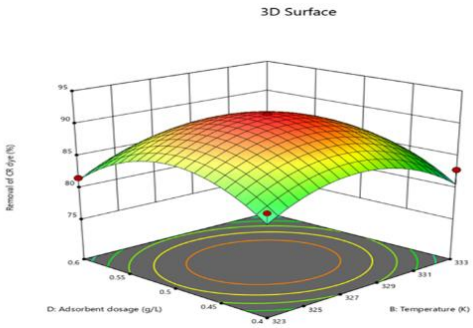


Fig. 45. Response surface plot of adsorbent dosage vs temperature on % dye removal of CR.

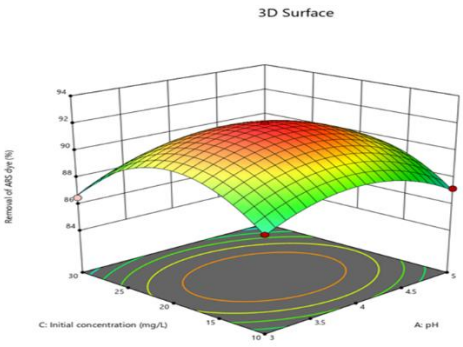


Fig. 46. Response surface plot of initial concentration vs solution pH on % dye removal of ARS.

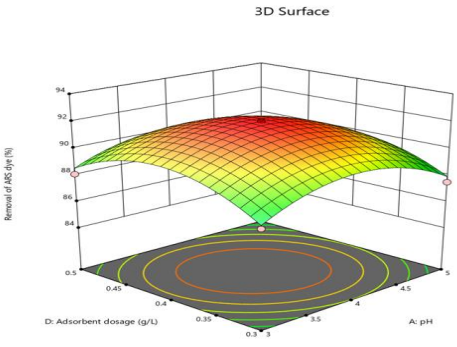


Fig. 47. Response surface plot of adsorbent dosage vs solution pH on % dye removal of ARS.

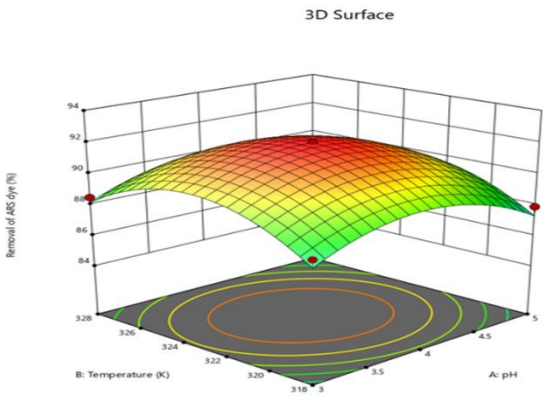


Fig. 48. Response surface plot of temperature vs solution pH on % dye removal of ARS.

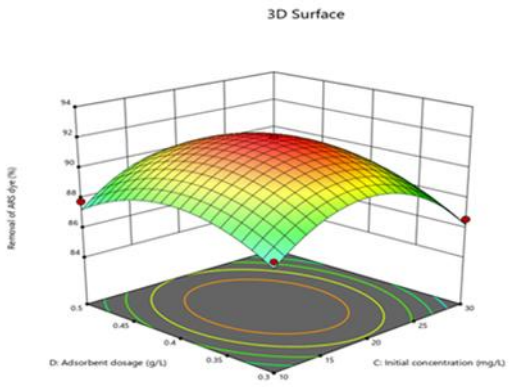


Fig. 49. Response surface plot of initial concentration vs adsorbent dosage on % dye removal of ARS.

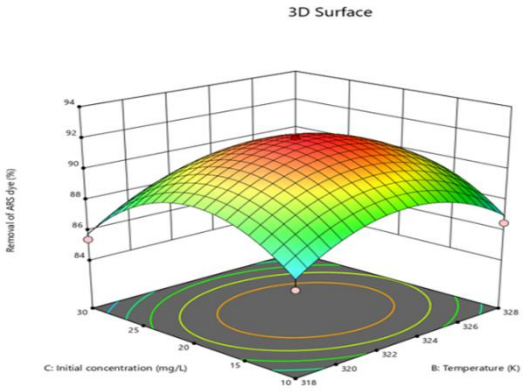


Fig. 50. Response surface plot of initial concentration vs temperature on % dye removal of ARS.

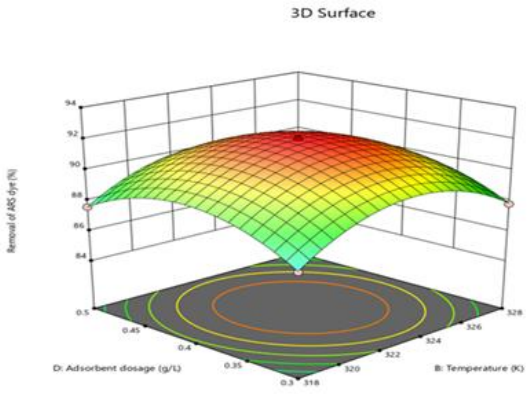


Fig. 51. Response surface plot of temperature vs adsorbent dosage on % dye removal of ARS.

Response surface contour plots are valuable tools for better understanding variable interactions. When other variables are held constant, these plots depict how any two factors jointly influence the response. The shape of the response surface offers insights into the nature of the interactions: a circular surface indicates no interaction, while elliptical shapes suggest strong interactions. The smallest elliptical contour that encloses the highest percentage of dye removal represents the optimal combination of process variables. (Fig. 52 -63) present these contour plots for the combined effects of process factors on dye removal efficiency for ARS and CR, respectively.

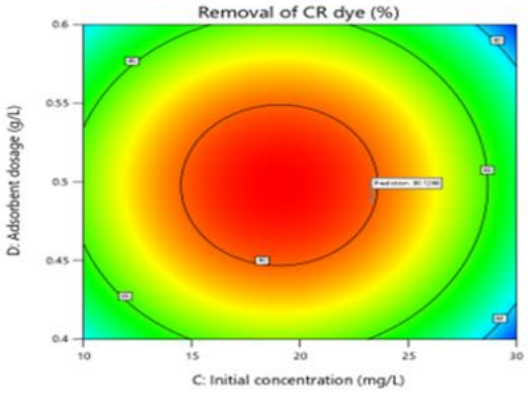


Fig. 52. Contour plot of initial concentration vs adsorbent dosage on % dye removal of CR.

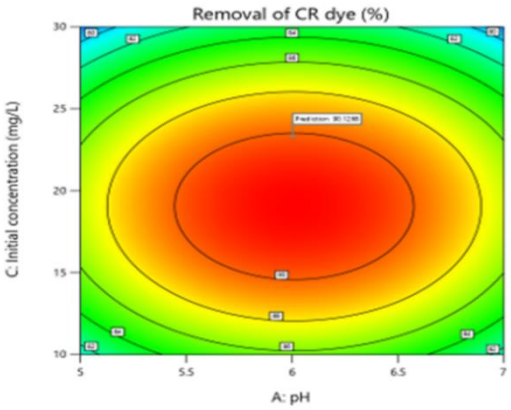


Fig. 53. Contour plot of initial concentration vs solution pH on % dye removal of CR.

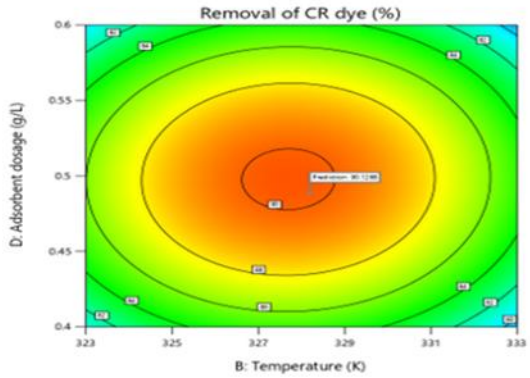


Fig. 54. Contour plot of temperature vs adsorbent dosage on % dye removal of CR.

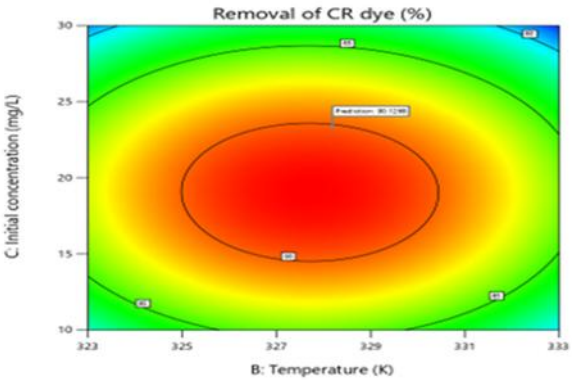


Fig. 55. Contour plot of initial concentration vs temperature on % dye removal of CR.

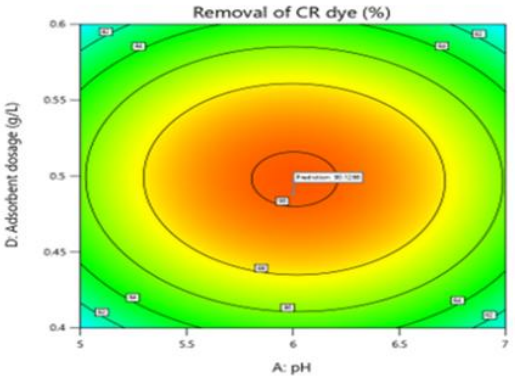


Fig. 56. Contour plot of adsorbent dosage vs pH on % dye removal of CR.

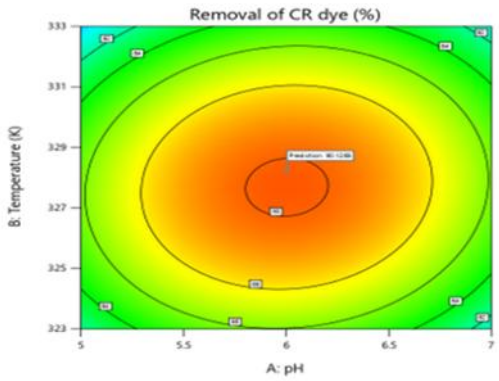


Fig. 57. Contour plot of solution pH vs temperature on % dye removal of CR.

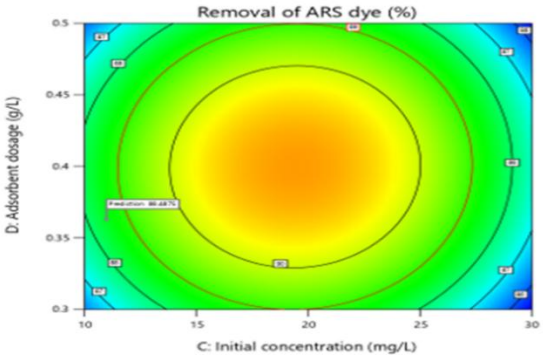


Fig. 58. Contour plot of initial concentration vs adsorbent dosage on % dye removal of ARS.

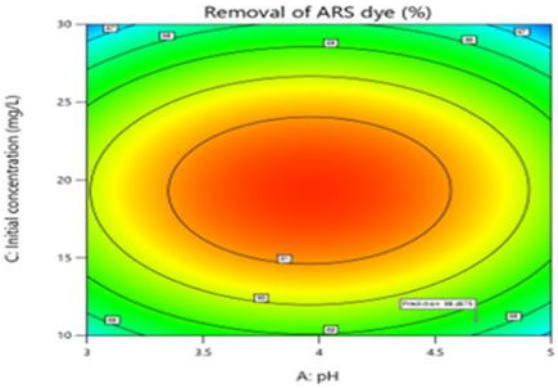


Fig. 59. Contour plot of initial concentration vs solution pH on % dye removal of ARS.

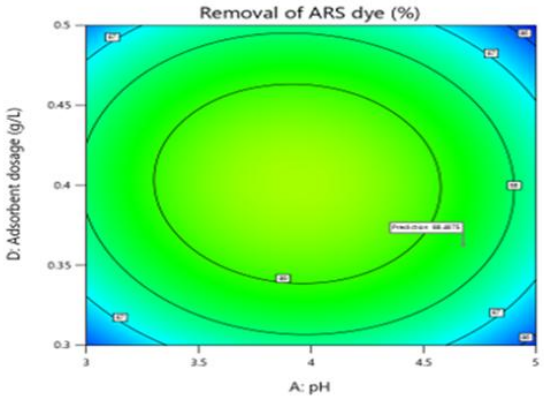


Fig. 60. Contour plot of adsorbent dosage vs solution pH on % dye removal of ARS.

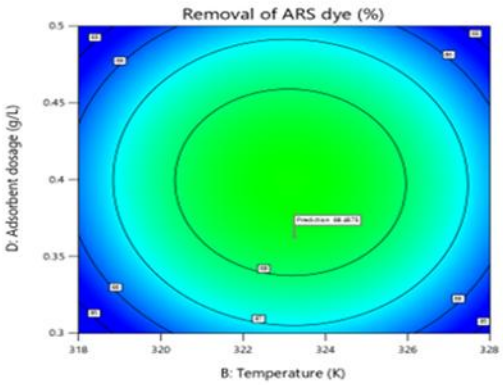


Fig. 61. Contour plot of adsorbent dosage vs temperature on % dye removal of ARS.

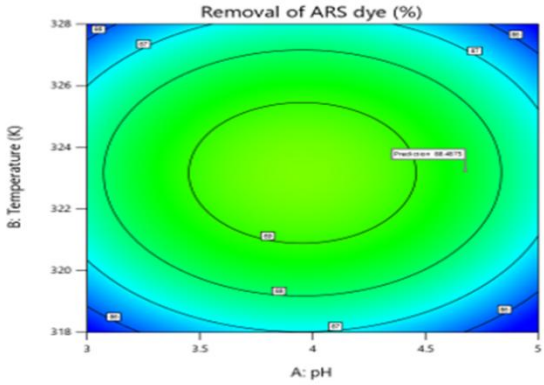


Fig. 62. Contour plot of pH vs temperature on % dye removal of ARS.

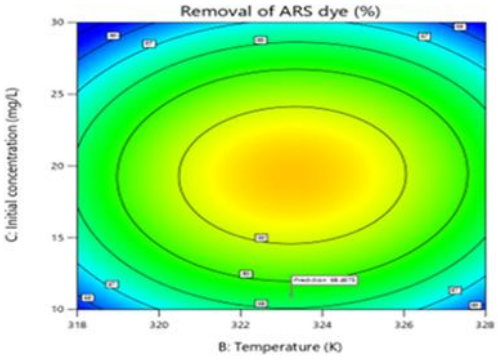


Fig. 63. Contour plot of initial concentration vs temperature on % dye removal of ARS.

4. CONCLUSION

In this study, Congo Red and Alizarin Red S dyes were extracted from aqueous solutions using Iron Oxide nanoparticles derived from Litchi chinensis Peels (LC-Fe_2O_3-NPs). SEM, XRD, BET, XPS, and FTIR techniques were used to characterize the adsorbents, and batch adsorption tests confirmed by response surface methodology were used to evaluate their efficacy. For both dyes, the contact time with LC-Fe_2O_3-NPs achieved equilibrium after 30 minutes. The ideal adsorbent dose for LC-Fe_2O_3-NPs was 0.4 g/L. The pH of the solution was crucial; Congo Red removal required a pH of 6, whereas Alizarin Red S removal required a pH of 4. At 328 K, the highest adsorption efficiency was reached. LC-Fe_2O_3-NPs eliminated Congo Red and Alizarin Red S with efficiencies of 95.62% and 96%, respectively, at an initial dye concentration of 10 mg/L. The maximum adsorption capabilities of LC-Fe_2O_3-NPs for Congo Red and Alizarin Red S dyes were 171.23 mg/g and 186.66 mg/g, respectively. The Freundlich isotherm model best described the adsorption behavior, according to equilibrium data analysis. This suggests a heterogeneous surface with multilayer adsorption that includes both physisorption and chemisorption mechanisms. The adsorption process was accurately represented by the pseudo-second-order model, according to kinetic studies. The calculated enthalpy and entropy changes verified that the adsorption was endothermic, spontaneous, and feasible. Equilibrium data analysis revealed that the Freundlich isotherm model best explained the adsorption behavior. This implies a heterogeneous surface with multilayer adsorption involving chemisorption and physisorption processes. Kinetic experiments showed that the pseudo-second-order model accurately described the adsorption process. The endothermic, spontaneous, and practicable nature of the adsorption was confirmed by the computed enthalpy and entropy changes. The experimental results convincingly show that LC-Fe_2O_3-NPs are very efficient and inexpensive adsorbents for removing Congo Red and Alizarin Red S dyes from wastewater. Their excellent adsorption properties, combined with the use of agricultural waste as precursor materials, make bio-synthesized nanoparticles viable candidates for long-term wastewater treatment applications. For adsorption applications, the generated nanoparticles' structural features were advantageous. Particles with irregular shapes and sizes smaller than 100 nm were found via SEM analysis. The adsorbent's crystalline and porous structure, which contributed to its enormous surface area, was confirmed by XRD, BET, and XPS analysis. Several functional groups (hydroxyl, carboxyl, and amino groups) on the adsorbent surfaces were identified by FTIR spectroscopy as aiding dye molecule binding through chemical bonding and electrostatic interactions. The Box-Behnken design response surface methodology effectively modified important process variables like temperature, pH, adsorbent dosage, and initial dye concentration. The statistical model's dependability for process optimization was demonstrated by the excellent agreement between the predicted values from Response Surface Methodology (RSM) and the experimental findings.

Acknowledgements

The authors thank the Dept. of Chemical Engg., Andhra University College of Engg, Visakhapatnam, for providing laboratory facilities and academic support. Special appreciation is extended to Prof. Pulipati King and Prof. Meena Vangalapati for their guidance. AI assistance was used solely to improve language clarity, and the final manuscript was fully reviewed and approved by the authors.

Author contributions

Sivakumar Bandaru: Writing-Original Draft, Conceptualization, Investigation. Tamirat Lamaro Bate: Writing, Review, and Editing. Megersa Taddesse Adugna: Review and Editing. Velaga P V S Sai Pranai: Review and Editing. A. Narendra Kumar: Review and Editing. Pulipati King: Supervision, Methodology, and Validation. Meena Vangalapati: Supervision, Methodology, and Validation.

Funding Declaration

The authors declare that no funding was received for this study.

Data availability statement

All data generated or analyzed during this study are included in this published article

REFERENCES

1. Afkhami, A., Saber-Tehrani, M., & Bagheri, H., Simultaneous removal of heavy-metal ions in wastewater samples using nano-alumina modified with 2,4-dinitrophenylhydrazine. Journal of Hazardous Materials, 181(1-3), 836-844. https://doi.org/10.1016/j.jhazmat.2010.05.089 (2010).
2. Ahmad, I.Z., Ahmad, A., Tabassum, H., Kuddus, M.: Applications of nanoparticles in the treatment of wastewater. In: Handbook of Ecomaterials. pp. 275–299 https://doi.org/10.1007/978-3-319-48281-1_37-1 (2019)
3. Prasad, K.S., Gandhi, P., Selvaraj, K.: Synthesis of green nano iron particles (GnIP) and their application in adsorptive removal of As(III) and As(V) from aqueous solution. Appl. Surf. Sci. 317, 1052–1059 http://dx.doi.org/10.1016/j.apsusc.2014.09.042 (2014).
4. Saravanan, A., Kumar, P.S., Karishma, S., Vo, D.V.N., Jeevanantham, S., Yaashikaa, P.R., George, C.S.: A review on biosynthesis of metal nanoparticles and its environmental applications. Chemosphere. 264, 128580 https://doi.org/10.1016/j.chemosphere.2020.128580 (2021).
5. Vikrant, K., Giri, B.S., Raza, N., Roy, K., Kim, K.H., Rai, B.N., Singh, R.S.: Recent advancements in bioremediation of dye: Current status and challenges. Bioresour. Technol. 253, 355–367 https://doi.org/10.1016/j.biortech.2018.01.029 (2018).
6. Selvaraj, V., Swarna Karthika, T., Mansiya, C., Alagar, M.: An over review on recently developed techniques, mechanisms and intermediate involved in the advanced azo dye degradation for industrial applications. J. Mol. Struct. 1224, 129195 https://doi.org/10.1016/j.molstruc.2020.129195 (2021).
7. Benkhaya, S., M'rabet, S., El Harfi, A.: Classifications, properties, recent synthesis and applications of azo dyes. Heliyon. 6, https://doi.org/10.1016/j.heliyon.2020.e03271 (2020).
8. Baban, A., Yediler, A., Lienert, D., Kemerdere, N., Kettrup, A.: Ozonation of high strength segregated effluents from a woollen textile dyeing and finishing plant. Dye. Pigment. 58, 93–98 https://doi.org/10.1016/S0143-7208(03)00047-0 (2003).
9. Saratale, R.G., Saratale, G.D., Kalyani, D.C., Chang, J.S., Govindwar, S.P.: Enhanced decolorization and biodegradation of textile azo dye Scarlet R by using developed microbial consortium-GR. Bioresour. Technol. 100, 2493–2500 https://doi.org/10.1016/j.biortech.2008.12.013 (2009).
10. Berradi, M., Hsissou, R., Khudhair, M., Assouag, M., Cherkaoui, O., El Bachiri, A., El Harfi, A.: Textile finishing dyes and their impact on aquatic environs. Heliyon. 5, https://doi.org/10.1016/j.heliyon.2019.e02711 (2019).
11. Kehinde, F., Aziz, H.A.: Textile Waste Water and the advanced Oxidative Treatment Process, an Overview. Int. J. Innov. Res. Sci. Eng. Technol. 03, 15310–15317 https://doi.org/10.15680/IJIRSET.2014.0308034 (2014).
12. Sharma, K.P., Sharma, S., Sharma, S., Singh, P.K., Kumar, S., Grover, R., Sharma, P.K.: A comparative study on characterization of textile wastewaters (untreated and treated) toxicity by chemical and biological tests. Chemosphere. 69, 48–54 https://doi.org/10.1016/j.chemosphere.2007.04.086 (2007).
13. Sekomo, C.B., Rousseau, D.P.L., Saleh, S.A., Lens, P.N.L.: Heavy metal removal in duckweed and algae ponds as a polishing step for textile wastewater treatment. Ecol. Eng. 44, 102–110 https://doi.org/10.1016/j.ecoleng.2012.03.003 (2012).
14. Solís, M., Solís, A., Inés, H., Manjarrez, N., Flores, M.: Microbial decolouration of azo dyes : A review. Process Biochem. 47, 1723–1748 https://doi.org/10.1016/j.procbio.2012.08.014 (2012).
15. Kumar, S., Raut, S., Bandyopadhyay, P.: Fungal decolouration and degradation of azo dyes : A review. Fungal Biol. Rev. 30, 112–133 https://doi.org/10.1016/j.fbr.2016.06.003
16. Yaseen, D.A., Scholz, M.: Shallow pond systems planted with Lemna minor treating azo dyes. Ecol. Eng. 94, 295–305 (2016). http://dx.doi.org/10.1016/j.ecoleng.2016.05.081 (2016).
17. Wu, Y., Pang, H., Liu, Y., Wang, X., Yu, S., Fu, D., Chen, J., Wang, X.: Environmental remediation of heavy metal ions by novel-nanomaterials : A review *. Environ. Pollut. 246, 608–620 https://doi.org/10.1016/j.envpol.2018.12.076 (2019).
18. Kaur, Sumanjit, Seema Rani, and Rakesh Kumar Mahajan. "Adsorption kinetics for the removal of hazardous dye congo red by biowaste materials as adsorbents." Journal of chemistry 2013 https://doi.org/10.1155/2013/628582 (2013).
19. Cyclic Sequential Removal of Alizarin Red S Dye and Cr(VI) Ions Using Wool as a Low-Cost Adsorbent Mustafa I. Khamis , Taleb H. Ibrahim , Fawwaz H. Jumean , Ziad A. Sara and Baraa A. Atallah https://doi.org/10.3390/pr8050556?urlappend=%3Futm_source%3Dresearchgate.net%26utm_medium%3Darticle
20. Gholivand, Mohammad Bagher, et al. "Adsorptive removal of alizarin red-S and alizarin yellow GG from aqueous solutions using polypyrrole-coated magnetic nanoparticles." Journal of Environmental Chemical Engineering 3.1 (2015): 529-540. https://doi.org/10.1016/j.jece.2015.01.011 (2015)
21. Makarov, V. V., Love, A. J., Sinitsyna, O. V., Makarova, S. S., Yaminsky, I. V., Taliansky, M. E., & Kalinina, N. O.. "Green" nanotechnologies: Synthesis of metal nanoparticles using plants. Acta Naturae, 6(1), 35-44. https://doi.org/10.32607/20758251-2014-6-1-35-44 (2014)
22. Jia Wu, Jianwei Yang, Pu Feng, Guohuan Huang, Chuanhui Xu, Baofeng Lin, High-efficiency removal of dyes from wastewater by fully recycling litchi peel biochar, Chemosphere, 246, https://doi.org/10.1016/j.chemosphere.2019.125734 (2020).

23. Manzoor, K., Batool, M., Naz, F. et al. A comprehensive review on application of plant-based bioadsorbents for Congo red removal. Biomass Conv. Bioref. 14, 4511–4537 https://doi.org/10.1007/s13399-022-02741-5 (2024).
24. Joshua N. Edokpayi, Emmanuel Makete, Removal of Congo red dye from aqueous media using Litchi seeds powder: Equilibrium, kinetics and thermodynamics, Physics and Chemistry of the Earth, Parts A/B/C, 123 https://doi.org/10.1016/j.pce.2021.103007, (2021).
25. Estevan D. Cruz, Juliano Missau, Simon R. Collinson, Eduardo H. Tanabe, Daniel A. Bertuol, Efficient removal of congo red dye using activated lychee peel biochar supported Ca-Cr layered double hydroxide, Environmental Nanotechnology, Monitoring & Management, 20, https://doi.org/10.1016/j.enmm.2023.100835 (2023).
26. Nasser, A.O., Kareem, S.L. Removal of Congo red from aqueous solution using lemon peel-Fe3O4 nanocomposite adsorbent. Biomass Conv. Bioref. 14, 23183–23193 https://doi.org/10.1007/s13399-023-04496-z?urlappend=%3Futm_source%3Dresearchgate.net%26utm_medium%3Darticle (2024).
27. Bahman Ramavandi, Ali Asghar Najafpoor, Hossein Alidadi, Ziaeddin Bonyadi, Alizarin red-S removal from aqueous solutions using Saccharomyces cerevisiae: kinetic and equilibrium study, Desalination and Water Treatment, 144, 286-291, https://doi.org/10.5004/dwt.2019.23556 (2019)
28. Gautam PK, Shivapriya PM, Banerjee S, Sahoo AK, Samanta SK. Biogenic fabrication of iron nanoadsorbents from mixed waste biomass for aqueous phase removal of alizarin red S and tartrazine: Kinetics, isotherm, and thermodynamic investigation. Environ Prog Sustainable Energy.; 39:e13326.https://doi.org/10.1002/ep13326 (2020)
29. Ruixue Jiang, Jiyu Tian, Hao Zheng, Jinqiu Qi, Shujuan Sun, Xiaochen Li, A novel magnetic adsorbent based on waste litchi peels for removing Pb(II) from aqueous solution, Journal of Environmental Management, 155, 24-30, https://doi.org/10.1016/j.jenvman.2015.03.009 (2015)
30. Foletto, V.S., Ferreira, A.B., da Cruz Severo, E. et al. Iron-based adsorbent prepared from Litchi peel biomass via pyrolysis process for the removal of pharmaceutical pollutant from synthetic aqueous solution. Environ Sci Pollut Res 24, 10547–10556 https://doi.org/10.1007/s11356-017-8745-7?urlappend=%3Futm_source%3Dresearchgate.net%26utm_medium%3Darticle (2017).
31. J. Zolgharnein, Z. Choghaei, M. Bagtash, Sh. Feshki, M. Rastgordani & P. Zolgharnein: Nano-Fe_3O_4 and corn cover composite for removal of Alizarin Red S from aqueous solution: characterization and optimization investigations, Desalination and Water Treatment. https://doi.org/10.1080/19443994.2016.1177736 (2016).
32. Sustainable Synthesis of Ananas Comosus (Pineapple Peel)-Zinc Nanoparticles (PA-Zn Nps) for Congo Red Dye Remediation S Bandaru, P King, M Vangalapati Eurasian Journal of Analytical Chemistry 12 (3), 11-21 https://doi.org/10.1080/21870764.2022.2127504 (2022).
33. ENHANCED METHYLENE BLUE ADSORPTIVE REMOVAL BY GREEN-SYNTHESIZED Litchi chinensis-SEED COPPER NANOPARTICLES UPON RSM OPTIMIZATION: KINETIC AND ISOTHERM PERSPECTIVES PA Kumar, AS Juttuka, M Sudheera, P King, DA Naidu, M Vangalapati https://doi.org/10.31788/RJC.2026.1919585 (2026).
34. Kinetic, Thermodynamic and Equilibrium Studies for the Biosorption of Nickel from an aqueous solution on to Ipomea palmata Leaves powder K Kumaraswamy, P King, YP Kumar Research Journal of Pharmacy and Technology 10 (9), 3029-3034 https://doi.org/10.5958/0974-360X.2017.00538.8 (2017).
35. Sustainable synthesis and characterization of Zn–Al doped nanocomposites for removal of brilliant blue dye: optimization using a response surface methodology S Matla, G Talathoti, TL Bate, MT Adugna, P Yogitha, B Reddemma, .Scientific Reports 15 (1), 41286 https://doi.org/10.1038/s41598-025-25078-1 (2025).
36. Sustainable Synthesis of Zn/Al-Doped Nanocomposite from Bio-Waste: Characterization and RSM-Guided Brilliant Blue Dye Adsorption Optimization S Matla, G Talathoti, MT Adugna, TL Bate, P King, M Vangalapati https://doi.org/10.21203/rs.3.rs-7414495/v1 (2025).
37. Synthesis and characterization of Titanium doped activated carbon nanoparticles and its application for the removal of dicofolSI Vali, U Sirisha, VR Poiba, M Vangalapati, P King Materials Today: Proceedings 44, 2290-2295 https://doi.org/10.1016/J.MATPR.2020.12.392 (2021).
38. Biosorption of congo red dye from aqueous solutions using synthesized silver nano particles of Grevillea robusta: Kinetic studies P VenkataRao, G SaiTarun, C Govardhani, B Manasa, PJ Joy, ...Materials Today: Proceedings 26, 3009-3014 https://doi.org/10.1016/j.matpr.2020.02.626 (2020).
39. Catalytic Activity of Nanocomposite: Synthesized Electrochemical Sludge using Iron Electrodes and Marine Algae (Fe_3 O_4/marine algae NP) for the Degradation of Emerging …V Supriya, VR Poiba, M Vangalapati NanoWorld J 9 (2), 29-36 https://doi.org/10.17756/nwj.2023-114 (2023).
40. Copper-Doped Zinc Oxide Nanoparticles: Synthesis, Characterization, and Application for Adsorptive Removal of Toxic Azo Dye B Sowjanya, P King, M Vangalapati, VR Myneni International Journal of Chemical Engineering (1), 8640288 https://doi.org/10.1155/2023/8640288 (2023).